SPIN-ORBIT COUPLING IN STRONGLY CORRELATED SYSTEMS

A Dissertation
Submitted to
the Temple University Graduate Board

In Partial Fulfillment
of the Requirements for the Degree
DOCTOR OF PHILOSOPHY

---

by
Xiao Yuan
May 2022

Examining Committee Members:

Peter S. Riseborough, Advisory Chair, Physics
Andreas Metz, Physics
Qimin Yan, Physics
Spiridoula Matsika, External Member, Chemistry, Temple University

ABSTRACT

In materials with heavy elements, both strong spin-orbit coupling and Coulomb interactions are possible to exist. Both can significantly change the properties of materials. The coexistence of them can induce more interesting phenomena in solids. In this dissertation, three different cases involved with spin-orbit coupling and Coulomb interaction are separately studied. In the first case, impurity states in topological Kondo insulators are studied. Both in-gap and deep-bound impurity states are explicitly examined. The in-gap impurity states have properties similar to those of the topological surface states. It can explain some anomalous properties observed in SmB_6, a possible topological Kondo insulator. In the second one, it is proposed that spin-orbit coupling can be strongly enhanced by Coulomb interaction in $5f$ metals. Modest values of the Coulomb interaction can induce up to a four-fold enhancement. In the third case, a model is presented to characterize spin-orbit enhancement in a strongly correlated two-dimensional system. By our calculation, it is shown that a possible nonlinear Rashba effect can emerge in such a system. It can explain the presence of giant Rashba constants in some two-dimensional devices.

DEDICATION

To my beloved *Chao Yang*

ACKNOWLEDGEMENTS

Firstly, I would like to give a lot of thanks to my advisor Peter S. Riseborough. Without his help, it would be impossible for me to do so much research work in a relatively short time. Secondly, I would like to show my appreciation to all the teachers who taught me various courses during my Temple time, especially Andreas Metz who taught me elementary particle physics. Under their delicate education, I become familiar with different topics of physics. Finally, I also want to mention all my friends, Yiran Li, Shiqi Ruan, Xu Zhang, and Zack, who I get accustomed to in Philadelphia. Without knowing them, life would have been less interesting.

TABLE OF CONTENTS

LIST OF FIGURES

LIST OF TABLES

CHAPTER 1

INTRODUCTION

Since the Schrödinger equation was postulated in 1925, all quantum physics above the atom scale should be fairly understood. Condensed matter physics, which apparently falls into this scale, enjoys its fast development since then with numerous phenomena discovered and successfully explained. However, it is not easy to solve a model Hamiltonian in a many-body system even with only two parameters such as the Hubbard model [1], which beyond the one-dimensional case no analytical solutions have been found. One reason behind such a difficulty to reach a full solution in many-body systems is that different interactions tend to lead to different ground states. In the case of the Hubbard model , the kinetic energy and the repulsion energy compete, leading to the metal-insulator transition. Even though it is difficult to treat such transitions in all parameter spaces, it is much easier to solve the problem by using such as perturbation theory if we know the ground state of the particular case. In this dissertation, we employ techniques such Green's function and perturbation theory to study three separate concrete cases involved with both spin-orbit coupling and strong correlation.

1.1 Spin-orbit Coupling in Solids

The spin-orbit coupling is first introduced in atom physics, in which an electron's spin and its motion around the nucleus are coupled through the Coulomb interaction. It is a pure relativistic effect, where a fast-moving electron sees an effective magnetic field which interacts with its magnetic moment. An electron in an atom has a quantized orbital angular momentum number and a spin angular momentum number. Different combinations of them lead to different total angular momentum numbers with different energies because of the spin-orbit coupling, which gives rise to the so-called fine structure. It is even more interesting when the spin-orbit coupling emerges in solids. In the band theory picture, electrons have well-defined momenta which can couple with electrons' intrinsic spins. Due to different symmetries of various solids, the spin-orbit coupling manifests itself in different ways such as the Dresselhaus effect and the Rashba effect [2]. It makes applications in spintronics very attractive since it makes it possible to manipulate electrons' spins in solid devices [3]. One significant example is that because of the existed Rashba field, injected spin-polarized electrons can acquire phase by spin precessing, which leads to spin interference when electrons pass through devices. The interference can be controlled by changing the electric field, which can be observed in transport experiments. In recent years, the spin-orbit coupling is attracting even more attention because of the theoretical predication of topological insulators and the experimental confirmation of them [4], in which the spin-orbit coupling plays a dominant role . In a system of time-reversal symmetry, Kramers theorem ensures two-fold degeneracy at time-reversal points, while spin-orbit coupling lifts such degeneracy away from those points. Nontrivial connections between Kramers partners can lead to the formation of topological insulators which have protected edge states.

1.2 Electron-electron Correlation

Electrons always interact with each other by the long-range Coulomb interaction. In this regard, electrons in any bulk material should show strong correlations owing to the positions and momenta of all other electrons. However, in many materials, electronic correlations can be ignored. In simple metals, a free Fermi gas model, which ignores all correlations, captures all the important physics of such systems. A more realistic theory, Landau's Fermi liquid theory, which includes some correlations, accounts for the properties of normal metals very well. Band theory, which more or less treats different orbitals of atoms independently in materials, can categorize different materials into metals (semimetals), semiconductors and insulators. The most important properties of particular materials can be extracted from their electronic band structures, especially after modern density functional theory is well developed, which makes the calculation of materials not only qualitatively correct but also quantitatively accurate.

However, ignoring correlations might lead to wrong predictions in some cases. One of the most prominent example is NiO, which should be a metal according to the band theory but turns out to be an insulator. The explanation for this anomaly was given by Sir Nevill Mott by including strong electron-electron repulsion. The first and most simple model to describe it is the Hubbard model. The whole class of materials that become insulators because of strong electron-electron repulsion are named Mott insulators. Normally, such materials have atoms with partially occupied d or f orbitals, since compared to s and p orbitals, they are much more localized, which normally causes strong intra-atomic Coulomb repulsion. Such electron-electron repulsion not only simply makes some materials insulating, but also leads to numerous emergent phenomena in various situations. Materials due to such correlations are

high-temperature superconductors, heavy-fermion materials, and Kondo insulators. Therefore, the key to studying correlated-electron systems is to analyze the strong on-site Coulomb repulsion. Many sophisticated methods like dynamic mean-field theory, LDA + U and quantum Monte Carlo are developed to deal with such problems.

1.3 Purpose and Organization of the Dissertation

This dissertation aims to explore how the spin-orbit coupling behaves in different strongly correlated electron systems. The main technique employed is the Green's function method, which will be explained in several appropriate places in the whole dissertation. In chapter 2, we study the impurity states in the topological Kondo insulators. Kondo insulators have highly renormalized bands as a result of strong correlations, with small hybridization gaps. Strong spin-orbit coupling can make some Kondo insulators topologically nontrivial, which have protected surface states. In our calculation, it is shown that the in-gap bound states have properties similar to those of the topological surface states. We also compare our results with the experimental observations to explain the mysteries of the topological Kondo insulator candidate SmB_6. The Dirac equation is introduced to illustrate how the spin-orbit coupling changes the parity of the wave function of a spherical void to help understand the impurity states in a topological insulator in appendix A. In chapter 3, we study the direct relation between the spin-orbit coupling and the Coulomb interaction in $5f$ metals. It turns out that a strong enhancement to the order around 4 is possible and an anisotropic spin-orbit enhancement should be observed in tetragonal materials. It can explain unexpected large spin orbit gaps in some compounds. In chapter 4, a spin-orbit coupling enhancement in a two-dimensional strongly correlated system is studied. The numerical results show that an unexpected nonlinear Rashba effect

may be observed in strongly correlated two-dimensional materials or surfaces. This discovery can help to design new devices with giant Rashba constants. In the last chapter, the main results are summarized and future work is proposed.

CHAPTER 2

IMPURITY STATES IN TOPOLOGICAL KONDO INSULATORS

In this chapter, the concept of topological Kondo insulators is briefly reviewed. We then study the impurity states in the topological Kondo insulators and show that there are two kinds of impurity states that are significantly different from each other. Finally, we try to reveal the mysteries behind SmB_6, a strong candidate as topological Kondo insulator, by our model. We also use the Dirac equation to facilitate the understanding of the physics behind it, which is presented in Appendix A. The main part of this chapter has been published [5].

2.1 A Brief Review of Topological Kondo Insulators

The Kondo effect is one of the most well-studied correlation effects in condensed matter physics. It is the consequence of the scattering between local moments within impurity atoms and conduction electrons, which leads to the resistivity increasing below certain temperatures in metals with magnetic impurities. The Kondo coupling

can be understood by the Anderson impurity model through the Schrieffer-Wolff transformation [6]. Simply speaking, the model captures the idea that conduction electrons can hybridize with orbitals in local moments, whereas the strong Coulomb interaction penalizes the occupancy of the orbitals by extra electrons. The impurity model can be generalized to a lattice version, called the Anderson lattice model (ALM), which is widely applied to heavy fermion systems and Kondo insulators. The Hamiltonian can be written as

$$\begin{aligned}\hat{H}_{ALM} = &\sum_{\mathbf{k},\alpha} \epsilon_d(\mathbf{k}) d^\dagger_{\mathbf{k},\alpha} d_{\mathbf{k},\alpha} + \sum_{i,\beta} \epsilon_f(\mathbf{k}) f^\dagger_{\mathbf{k},\beta} f_{\mathbf{k},\beta} \\ &+ \sum_{\mathbf{k},\alpha,\beta} \Big(V_{\alpha,\beta}(\mathbf{k}) d^\dagger_{\mathbf{k},\alpha} f_{\mathbf{k},\beta} + h.c. \Big) + \sum_{\alpha\neq\beta} \frac{U}{2} f^\dagger_{i,\alpha} f_{i,\alpha} f^\dagger_{i,\beta} f_{i,\beta}.\end{aligned} \tag{2.1}$$

In such systems, f electrons are typically more localized and form flat bands, while d electrons play the role of itinerant electrons so that they constitute broad bands. By mean-field method, we can map equation 2.1 onto a non-interacting one,

$$\hat{H} = \sum_{\mathbf{k},\alpha} \epsilon_d(\mathbf{k}) d^\dagger_{\mathbf{k},\alpha} d_{\mathbf{k},\alpha} + \sum_{i,\beta} \tilde{\epsilon}_f(\mathbf{k}) f^\dagger_{\mathbf{k},\beta} f_{\mathbf{k},\beta} + \sum_{\mathbf{k},\alpha,\beta} (\tilde{V}_{\alpha,\beta}(\mathbf{k}) d^\dagger_{\mathbf{k},\alpha} f_{\mathbf{k},\beta} + h.c.). \tag{2.2}$$

According to Ref. [7], an insulator with time-reversal symmetry and inversion symmetry can be classified by Z_2 index,

$$Z_2 = \prod_{\Gamma_i} \delta(\Gamma_i) = \pm 1, \tag{2.3}$$

in which $\delta(\Gamma_i)$ is the products of the parities of the occupied bands at the high-symmetry point Γ_i. It is predicted that the concept of topological insulator might apply to strongly correlated systems such as Kondo insulators [8] due to band inversion by hybridization and strong spin-orbit coupling. SmB_6 has then become a strong

candidate as the first topological Kondo insulator [9].

2.2 Model Hamiltonian

Since we know in topological Kondo insulators the band inversion is critical, the presence of nonmagnetic impurities are investigated. The Hamiltonian can be written as

$$\hat{H} = \hat{H}_0 + \hat{H}_I. \tag{2.4}$$

The first part describes the Anderson lattice model with renormalized parameters written as

$$\hat{H}_0 = \sum_{\mathbf{k},\alpha} \left(\epsilon_d(\mathbf{k}) d^\dagger_{\mathbf{k},\alpha} d_{\mathbf{k},\alpha} + E_{f,\alpha} f^\dagger_{\mathbf{k},\alpha} f_{\mathbf{k},\alpha} \right) + \sum_{\mathbf{k},\alpha} \left(V(\mathbf{k}) f^\dagger_{\mathbf{k},\alpha} d_{\mathbf{k},\alpha} + h.c. \right), \tag{2.5}$$

where $E_{f,\alpha}$ is a renormalized on-site energy of f electrons and $V(\mathbf{k})$ is a renormalized hybridization matrix element. The band width of the unhybridized conduction band is set as $2W$. The hybridization matrix element $V(\mathbf{k})$ is an odd function due to the parity natures of d electrons and f electrons. Then the unperturbed system is expected to have an indirect gap of order $\frac{V^2}{W}$. The second term describes the potential caused by an impurity at the origin $\mathbf{R} = (0, 0, 0)$,

$$\hat{H}_I = \frac{1}{N} \sum_{\mathbf{k},\mathbf{k'}} \Delta U f^\dagger_{\mathbf{k},\alpha} f_{\mathbf{k'},\alpha}, \tag{2.6}$$

where N is the number of total lattice sites and ΔU is the potential energy at the site $\mathbf{R}$.

2.3 Green's Functions

The time-dependent single-particle ff Green's function is defined by

$$G^{ff}_{\mathbf{k},\alpha;\mathbf{k}',\alpha'}(t) = -i\,\langle \hat{T} f_{\mathbf{k},\alpha}(t) f^{\dagger}_{\mathbf{k}',\alpha'}(0)\rangle\,. \tag{2.7}$$

$\hat{T}$ is Wick's time-ordering operator. Then the equation of motion is

$$i\frac{\partial}{\partial t}G^{ff}_{\mathbf{k},\alpha;\mathbf{k}',\alpha'}(t) = \delta(t)\delta_{\mathbf{k},\mathbf{k}'}\delta_{\alpha,\alpha'} - i\,\langle \hat{T}[f_{\mathbf{k},\alpha}(t), \hat{H}(t)] f^{\dagger}_{\mathbf{k}',\alpha'}(0)\rangle\,, \tag{2.8}$$

in which the commutators can be evaluated by the Green's function

$$G^{df}_{\mathbf{k},\alpha;\mathbf{k}',\alpha'}(t) = -i\,\langle \hat{T} d_{\mathbf{k},\alpha}(t) f^{\dagger}_{\mathbf{k}',\alpha'}(0)\rangle\,. \tag{2.9}$$

By Fourier transform, the ff Green's function can be defined by

$$G^{ff}_{\mathbf{k},\alpha;\mathbf{k}',\alpha'}(\omega) = \int_{-\infty}^{\infty} dt \exp{(i\omega t)} G^{ff}_{\mathbf{k},\alpha;\mathbf{k}',\alpha'}(t). \tag{2.10}$$

The poles of the Fourier transformed Green's functions are the excitation energies of the system. The Fourier transformed equations of motion form a closed algebraic set of equations consisting of

$$\begin{aligned}(\omega - E_{f,\alpha}) G^{ff}_{\mathbf{k},\alpha;\mathbf{k}',\alpha'}(\omega) = \delta_{\mathbf{k},\mathbf{k}'}\delta_{\alpha,\alpha'} + V(\mathbf{k}) G^{df}_{\mathbf{k},\alpha;\mathbf{k}',\alpha'}(\omega) \\ + \frac{1}{N}\sum_{\mathbf{k}''} \Delta U G^{ff}_{\mathbf{k}'',\alpha;\mathbf{k}',\alpha'}(\omega)\end{aligned} \tag{2.11}$$

and

$$(\omega - \epsilon(\mathbf{k})) G^{df}_{\mathbf{k},\alpha;\mathbf{k}',\alpha'}(\omega) = V^{*}(\mathbf{k}) G^{ff}_{\mathbf{k},\alpha;\mathbf{k}',\alpha'}(\omega). \tag{2.12}$$

Combine the two equations above leads to

$$\begin{aligned}&\left(\omega - E_{f,\alpha} - \frac{|V(\mathbf{k})|^2}{\omega - \epsilon(\mathbf{k})}\right) G^{ff}_{\mathbf{k},\alpha;\mathbf{k}',\alpha'}(\omega) \\ &= \delta_{\mathbf{k},\mathbf{k}'}\delta_{\alpha,\alpha'} + \frac{1}{N}\sum_{\mathbf{k}''} \Delta U G_{\mathbf{k}'',\alpha;\mathbf{k}',\alpha'}(\omega).\end{aligned} \tag{2.13}$$

The ff Green's function in the absence of impurity is

$$G^{f,0}_{\mathbf{k},\alpha}(\omega) = \frac{(\omega - \epsilon(\mathbf{k}))}{(\omega - E_{f,\alpha})(\omega - \epsilon(\mathbf{k})) - |V(\mathbf{k})|^2}. \tag{2.14}$$

Then the ff Green's function can be solved in terms of T matrix

$$G^{ff}_{\mathbf{k},\alpha;\mathbf{k}',\alpha'}(\omega) = G^{ff,0}_{\mathbf{k},\alpha}(\omega)\delta_{\mathbf{k},\mathbf{k}'} + G^{ff,0}_{\mathbf{k},\alpha}(\omega) T_\alpha(\omega) G^{ff,0}_{\mathbf{k}',\alpha}(\omega), \tag{2.15}$$

where the T matrix is calculated by

$$T_\alpha(\omega) = \frac{\Delta U}{N}\frac{1}{1 - \frac{\Delta U}{N}\sum_{\mathbf{k}''} G^{f,0}_{\mathbf{k}'',\alpha}(\omega)}. \tag{2.16}$$

The time-dependent single-particle dd Green's function is defined by

$$G^{dd}_{\mathbf{k},\alpha;\mathbf{k}',\alpha'}(t) = -i\left\langle \hat{T} d_{\mathbf{k},\alpha}(t) d^\dagger_{\mathbf{k}',\alpha'}(0)\right\rangle. \tag{2.17}$$

Likewise, the df Green's function is

$$G^{fd}_{\mathbf{k},\alpha;\mathbf{k}',\alpha'}(t) = -i\left\langle \hat{T} f_{\mathbf{k},\alpha}(t) d^\dagger_{\mathbf{k}',\alpha'}(0)\right\rangle. \tag{2.18}$$

The Fourier transformed Green's functions have the coupled equations of motion

$$(\omega - \epsilon(\mathbf{k}))\, G^{dd}_{\mathbf{k},\alpha;\mathbf{k}',\alpha'}(\omega) = \delta_{\mathbf{k},\mathbf{k}'}\delta_{\alpha,\alpha'} + V^*(\mathbf{k}) G^{fd}_{\mathbf{k},\alpha;\mathbf{k}',\alpha'}(\omega) \tag{2.19}$$

and

$$(\omega - E_{f,\alpha})G^{fd}_{\mathbf{k},\alpha;\mathbf{k}',\alpha'}(\omega) = V(\mathbf{k})G^{df}_{\mathbf{k},\alpha;\mathbf{k}',\alpha'}(\omega) + \frac{1}{N}\sum_{\mathbf{k}''}\Delta U G^{fd}_{\mathbf{k}'',\alpha;\mathbf{k}',\alpha'}(\omega). \tag{2.20}$$

The unperturbed dd Green's function is

$$G^{d,0}_{\mathbf{k},\alpha}(\omega) = \frac{(\omega - E_{f,\alpha})}{(\omega - E_{f,\alpha})\,(\omega - \epsilon(\mathbf{k})) - |V(\mathbf{k})|^2}. \tag{2.21}$$

and fd one is

$$G^{fd,0}_{\mathbf{k},\alpha}(\omega) = \frac{V(\mathbf{k})}{(\omega - E_{fd,\alpha})\,(\omega - \epsilon(\mathbf{k})) - |V(\mathbf{k})|^2}. \tag{2.22}$$

In terms of T matrix, the full dd Green's function can be written by

$$G^{dd}_{\mathbf{k},\alpha;\mathbf{k}',\alpha'}(\omega) = G^{dd,0}_{\mathbf{k},\alpha}(\omega)\delta_{\mathbf{k},\mathbf{k}'} + G^{df,0}_{\mathbf{k},\alpha}(\omega)T_{\alpha}(\omega)G^{fd,0}_{\mathbf{k}',\alpha}(\omega). \tag{2.23}$$

2.4 Density of States

The total density of states can be evaluated by

$$\rho_T(\omega) = -\lim_{\eta\to 0^+}\frac{1}{\pi}\sum_{\mathbf{k},\alpha}\mathrm{Im}\left(G^{ff}_{\mathbf{k},\alpha;\mathbf{k},\alpha}(\omega + i\eta) + G^{dd}_{\mathbf{k},\alpha;\mathbf{k},\alpha}(\omega + i\eta)\right). \tag{2.24}$$

The total density of states can be separated into unperturbed part $\rho^0_T(\omega)$ and induced part $\Delta\rho_T(\omega)$ which is due to the presence of the impurity potential at the origin. The unperturbed part can be expressed by

$$\rho^0_T(\omega) = N\sum_{\alpha}\left(1 + \frac{V^2}{(\omega - E_{f,\alpha})^2}\right)\rho_{0,d}\left(\omega - \frac{V^2}{\omega - E_{f,\alpha}}\right), \tag{2.25}$$

where $\rho_{0,d}$ is the d electron density of states per site in the absence of hybridization. The density of states has two hybridized bands with a hybridization gap as shown in Fig. 2.1 . The change of the total density of states due to the impurity is

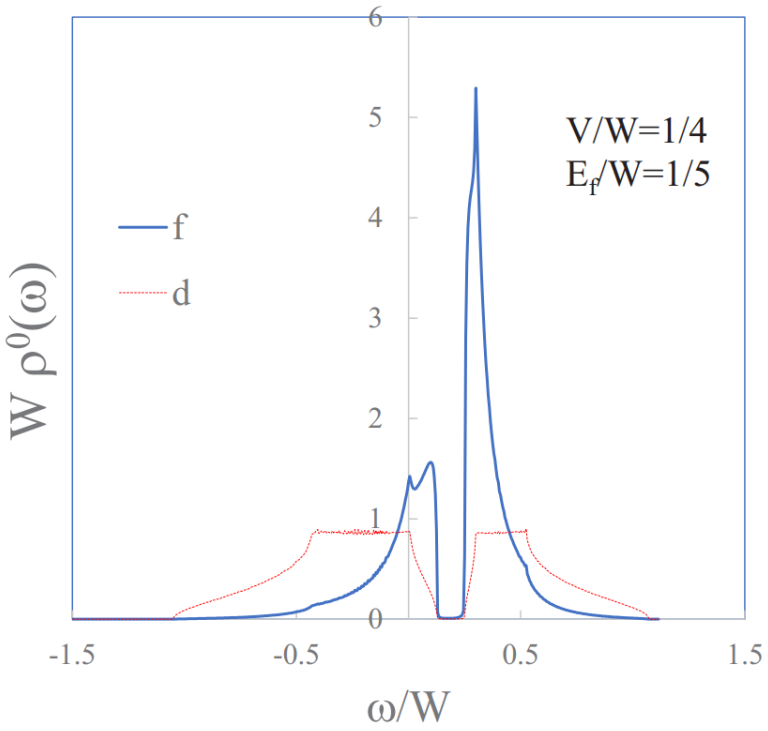

Figure 2.1: The unperturbed density of states of d electron and f electron. The f-binding energy is $E_{f,\alpha} = W/5$ and hybridization matrix element $V = W/4$. These values are not representative of SmB_6 but were chosen simply for clarity of illustration.

$$\begin{aligned}\Delta\rho_T(\omega) &= \lim_{\eta\to 0^+}\frac{1}{\pi}\sum_\alpha \mathrm{Im}\left(\frac{\frac{\Delta U}{N}\sum_{\mathbf{k}}\frac{\partial}{\partial\omega}G^{f,0}_{\mathbf{k},\alpha}(\omega+i\eta)}{1-\frac{\Delta U}{N}\sum_{\mathbf{k}}G^{f,0}_{\mathbf{k},\alpha}(\omega+i\eta)}\right)\\ &= \lim_{\eta\to 0^+}\frac{1}{\pi}\sum_\alpha \frac{\partial}{\partial\omega}\,\mathrm{Im}\ln T_\alpha(\omega+i\eta)\\ &= \frac{1}{\pi}\sum_\alpha\frac{\partial\delta_\alpha(\omega)}{\partial\omega},\end{aligned} \tag{2.26}$$

where $\delta(\omega)$ is the phase shift of the T matrix. This result accords with Friedel's theorem. The numerical density of states is shown in Fig. 2.2 . The integral of

$\Delta\rho_T(\omega)$ is zero because the total number of states is conserved in the Hilbert space. Passing by the position of the bound state, the phase shift jumps by π, indicating that the impurity state has a total spectral weight of unity.

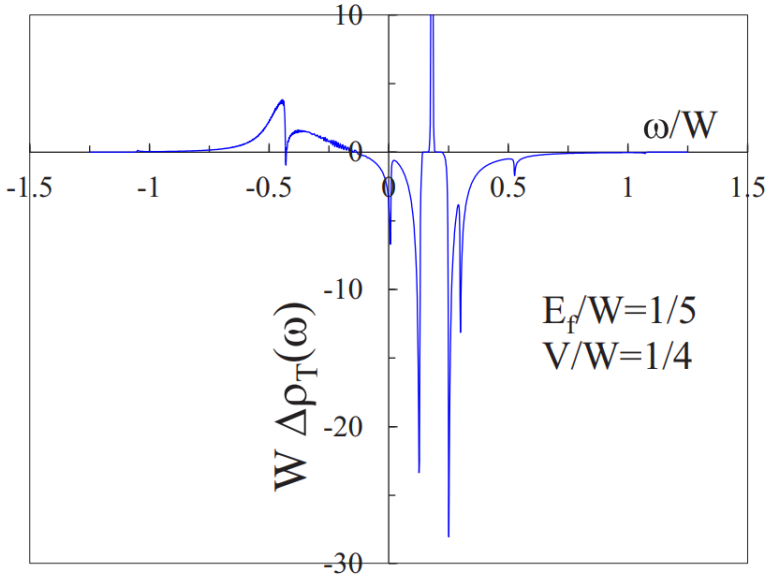

Figure 2.2: The change of the dimensionless total density of state due to the impurity. The value of ΔU was chosen as $-W/2$.

2.5 Bound States

For simplicity, we can set

$$\lim_{\eta\to 0^+} \mathrm{Re}\left(G^{f,0}_{\mathbf{k},\alpha}(\omega+i\eta)\right) = G^{Re,f}_{\mathbf{k},\alpha}, \tag{2.27}$$

$$\lim_{\eta\to 0^+} \mathrm{Im}\left(G^{f,0}_{\mathbf{k},\alpha}(\omega+i\eta)\right) = G^{Im,f}_{\mathbf{k},\alpha}. \tag{2.28}$$

Rewrite the induced density of states in a more informative form as

$$\begin{aligned}\Delta\rho_T(\omega) =& \frac{1}{\pi}\sum_{\alpha}\frac{\left(1-\frac{\Delta U}{N}\sum_{\mathbf{k}}G^{Re,f}_{\mathbf{k},\alpha}\right)\left(\frac{\Delta U}{N}\sum_{\mathbf{k}}\frac{\partial}{\partial\omega}G^{Im,f}_{\mathbf{k},\alpha}\right)}{\left(1-\frac{\Delta U}{N}\sum_{\mathbf{k}}G^{Re,f}_{\mathbf{k},\alpha}\right)^2+\left(\frac{\Delta U}{N}\sum_{\mathbf{k}}G^{Im,f}_{\mathbf{k},\alpha}\right)^2} \\ &+\frac{1}{\pi}\sum_{\alpha}\frac{\left(\frac{\Delta U}{N}\sum_{\mathbf{k}}G^{Im,f}_{\mathbf{k},\alpha}\right)\left(\frac{\Delta U}{N}\sum_{\mathbf{k}}\frac{\partial}{\partial\omega}G^{Re,f}_{\mathbf{k},\alpha}\right)}{\left(1-\frac{\Delta U}{N}\sum_{\mathbf{k}}G^{Re,f}_{\mathbf{k},\alpha}\right)^2+\left(\frac{\Delta U}{N}\sum_{\mathbf{k}}G^{Im,f}_{\mathbf{k},\alpha}\right)^2}.\end{aligned} \tag{2.29}$$

The numerical results are shown in Fig. 2.2. It is seen that impurity potential removes the spectral weight from the edges of the hybridization gap and forms an in-gap impurity state of weight unity. The ω-integrated total spectral weight is conserved. The in-gap state has the form of a delta function. ΔU is not sufficiently strong to produce a bound state below the lower hybridized band, but it is seen that the impurity potential has moved the spectral weight of the lower hybridized band to lower energies, thereby forming a virtual bound state with a Fano antiresonance.

The real and imaginary parts of the unperturbed ff Green's function over the momentum space can be evaluated by

$$\frac{1}{N}\sum_{\mathbf{k}}G^{Re,f}_{\mathbf{k},\alpha}=\frac{V^2}{(\omega-E_{f,\alpha})^2}\int d\epsilon\frac{\rho_{0,d}(\epsilon)}{\omega-\frac{V^2}{\omega-E_{f,\alpha}}-\epsilon}+\frac{1}{\omega-E_{f,\alpha}} \tag{2.30}$$

and

$$\frac{1}{N}\sum_{\mathbf{k}}G^{Im,f}_{\mathbf{k},\alpha}=-\frac{V^2}{(\omega-E_{f,\alpha})^2}\pi\rho_{0,d}\left(\omega-\frac{V^2}{\omega-E_{f,\alpha}}\right). \tag{2.31}$$

The unhybridized d electron density of states $\rho_{0,d}(\epsilon)$ is nonzero only within the energy width $-W<\epsilon<W$. However, for the nonmonotonic variation of the argument $\epsilon=\omega-\frac{V^2}{\omega-E_{f,\alpha}}$, ω within the hybridization gap forces the imaginary part to be zero. The numerical real and imaginary parts of the unperturbed ff Green's function are plotted in Fig. 2.3. The imaginary part has a continuous spectrum approaching an

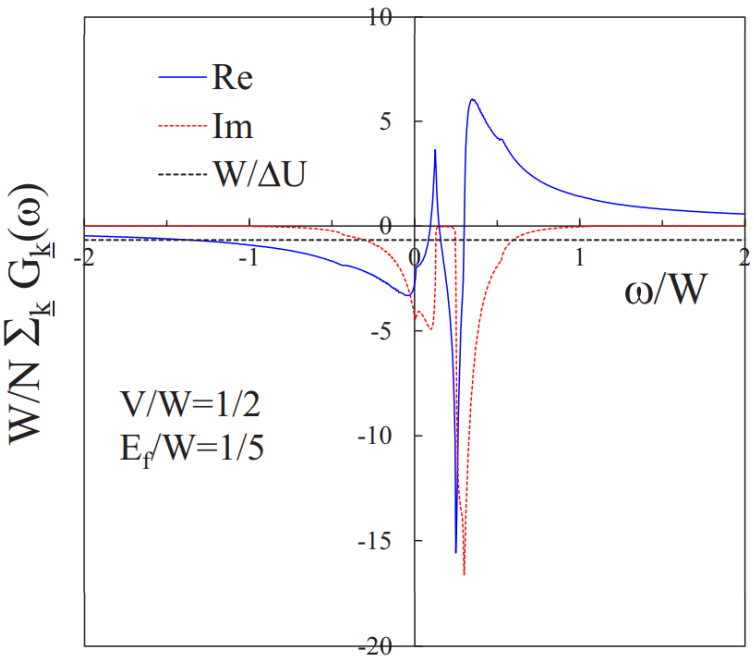

Figure 2.3: The real and imaginary parts of **k**-averaged dimensionless unperturbed ff Green's function. The values of $E_{f,\alpha}/W$ and V/W are chosen respectively as $1/5$ and $1/2$. Bound states occur at energies where $W/\Delta U$ shown by the horizontal dashed black line intersects with the blue line whenever the imaginary part (shown in red) is zero.

infinitesimal constant outside the f bandwidth and inside the hybridization gap. The bound state is likely to be found in these energy windows.

Within the gap at $\omega = E_{f,\alpha}$,

$$\frac{1}{N}\sum_{\mathbf{k}} G^{Im,f}_{\mathbf{k},\alpha} \sim -\frac{\eta}{N}\sum_{\mathbf{k}} \frac{V^2 + \left(E_{f,\alpha} - \epsilon(\mathbf{k})\right)^2}{V^4}, \tag{2.32}$$

so the imaginary part of the unperturbed ff Green's function is infinitesimal and its derivative is zero. The same conclusion can be reached by an alternate argument. The imaginary part can be generated by the replacement $\omega \to \omega + i\eta$ in the real part of the Green's function, $f(\omega)$, which is analytic and smoothly varying inside the

hybridization gap. By doing Taylor expansion to the first order, we have

$$f(\omega + i\eta) = f(\omega) + i\eta \frac{\partial f(\omega)}{\partial \omega} + \mathcal{O}(\eta^2). \tag{2.33}$$

As can be seen in Fig. 2.3, the real part is approximately linear, so the derivative of it will not only be infinitesimal but also approximately constant. Thus, the derivative of the imaginary part is expected to be negligibly small. Both arguments imply that, for the energies in the hybridized gap, the impurity contribution to the density of states only comes from the second term of Eq. 2.29, which reduces to

$$\Delta\rho_T(\omega) = -\frac{\Delta U}{N} \sum_{\mathbf{k},\alpha} \frac{\partial}{\partial \omega} G^{Re,f}_{\mathbf{k},\alpha} \delta \left(1 - \frac{\Delta U}{N} \sum_{\mathbf{k},\alpha} G^{Re,f}_{\mathbf{k},\alpha} \right). \tag{2.34}$$

For ω around $E_{f,\alpha}$, one finds that

$$\frac{1}{N} \sum_{\mathbf{k},\alpha} G^{Re,f}_{\mathbf{k},\alpha} \sim -\frac{\omega - \int d\epsilon \rho_{0,d}(\epsilon)\epsilon}{V^2}, \tag{2.35}$$

where the contributions from the simple poles at $\omega = E_{f,\alpha}$ have canceled. Therefore, due to the small magnitude of the hybridization gap and the asymmetry in the electron density of states, the real part of the Green's function varies rapidly in the gap. Its slope at $E_{f,\alpha}$ is approximately given by

$$-\frac{1}{N} \sum_{\mathbf{k},\alpha} G^{Re,f}_{\mathbf{k},\alpha} \sim \frac{1}{V^2} + \frac{E^2_{f,\alpha} + \int d\epsilon \rho_{0,d}(\epsilon)\epsilon^2}{V^4}. \tag{2.36}$$

As a result, the real part of the Green's function dips to a very large negative value below the upper edge of the hybridization gap and rises to a very large positive value just above the lower edge of the hybridization gap as shown in Fig. 2.3. Hence, even exceptionally small positive or negative values of ΔU are sufficient to produce

a solution of the equation

$$\frac{1}{\Delta U} = \frac{1}{N} \sum_{\mathbf{k},\alpha} G^{Re,f}_{\mathbf{k},\alpha}, \tag{2.37}$$

thereby producing zeros in the argument of the delta function of Eq. 2.34. Due to band inversion, positive values of ΔU slightly greater than a critical value produce in-gap bound states with energies just above the top of the hybridized valence band, whereas negative values of ΔU produce in-gap bound states just below the top of the hybridized conduction band. The spectral weight of the in-gap bound state is primarily removed from the closest edge of the hybridized band structure. For larger magnitudes of ΔU, the in-gap bound states shift away from the edges of the gap and the spectral weight is shifted to the bound states from both the upper and lower edges of the hybridization gap in almost equal proportions.

In addition to the bound states within the hybridization gap, sufficiently large values of ΔU can produce bound states either above or below the topmost or lowermost edge of the hybridized bands. The criterion for the production of a deep bound state is approximately given by

$$|\Delta U| > W. \tag{2.38}$$

The critical value of ΔU for the second type of states is expected to be of the order of eV, in contrast to the small critical value required to produce in-gap bound states.

2.6 Local Density of States

The number of f electrons at the site $\boldsymbol{R}$ is

$$\langle f^{\dagger}_{\mathbf{R},\alpha} f_{\mathbf{R},\alpha} \rangle = \frac{1}{N} \sum_{\mathbf{k},\mathbf{k}'} \exp\left(i(\mathbf{k}-\mathbf{k}')\cdot\boldsymbol{R}\right) \langle f^{\dagger}_{\mathbf{k},\alpha} f_{\mathbf{k}',\alpha} \rangle \,. \tag{2.39}$$

For the density of states, it can be evaluated by

$$\rho^f_{\mathbf{R}}(\omega) = -\frac{1}{\pi}\frac{1}{N}\lim_{\eta\to 0^+}\sum_{\mathbf{k},\mathbf{k}',\alpha}\exp\left(i(\mathbf{k}-\mathbf{k}')\cdot\boldsymbol{R}\right)\mathrm{Im}\left(G^{ff}_{\mathbf{k},\alpha;\mathbf{k}',\alpha}(\omega+i\eta)\right). \tag{2.40}$$

The expression for f-electron density of states at the impurity site is

$$\rho^f_{\mathbf{R}=0}(\omega) = \sum_{\alpha}\frac{1}{\Delta U}\delta\left(1-\frac{\Delta U}{N}\sum_{\mathbf{k}}G^{Re,f}_{\mathbf{k},\alpha}\right), \tag{2.41}$$

which has an explicit factor of $1/\Delta U$. The in-gap bound state has a spectral weight estimated to be $\frac{V^4}{W^2\Delta U^2}$. Therefore, in the limit $\Delta U \to \infty$, the in-gap bound state should vanish as expected. The different local densities of states for various values of ΔU are shown in Fig. 2.4. In addition to the in-gap bound states, the spectral weights of the continuum are seen to be shifted to lower energies. It is seen that the intensity of the in-gap bound state is very small and decreases as ΔU^{-2} when ΔU increases. For $\Delta U = -1.5W$, the bound state has split off from the bottom of the band and has removed almost all spectral weight from the continuous spectra. For $\Delta U = -0.5W$, an external bound state has not formed, but the on-site impurity potential has shifted spectral weight towards the bottom of the f band producing a virtual bound state.

The local f-electron density of state of the nearest neighbor site $\mathbf{R} = (1,0,0)$ is shown in Fig. 2.5. As the energy of the bound state approaches $E_{f,\alpha}$, the spectral weight increases towards a maximum value estimated to be $\frac{\frac{W^2}{36}}{V^2+E^2_{f,\alpha}+\frac{W^2}{6}}$. Hence, $\frac{1}{6}$ of the in-gap bound state spectral weight is of f-electron character which is equally distributed on the shell of nearest neighboring atoms. It is also can be seen that the spectral weights in the continuous portion of the spectrum for $\mathbf{R} = (1,0,0)$ are larger than those for the impurity site. Furthermore, as seen in Fig. 2.5, there is

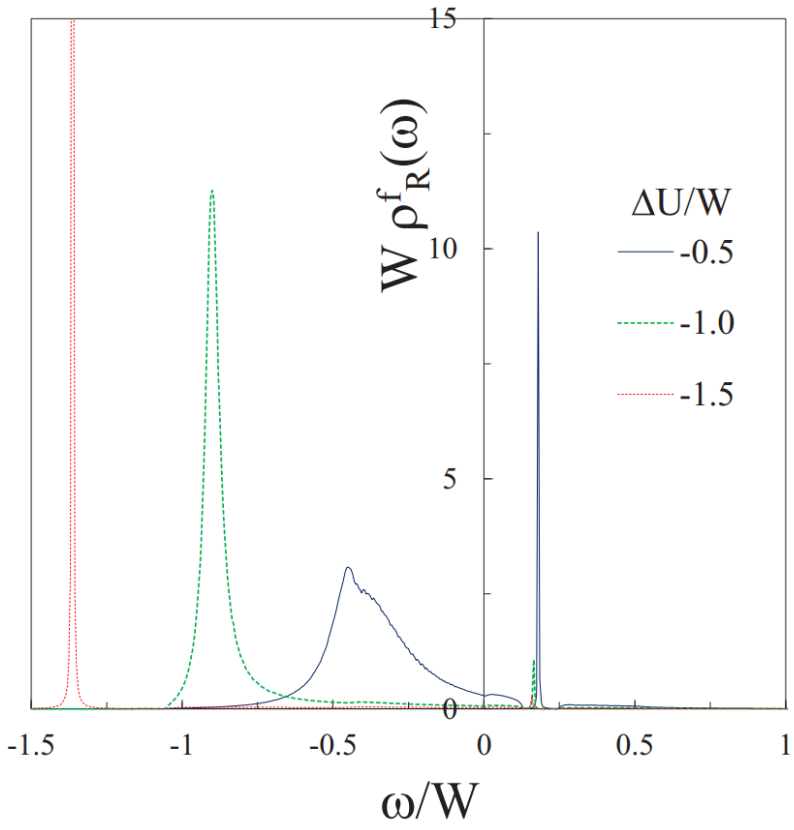

Figure 2.4: The dimensionless f-electron local densities of states of the impurity site for three values of ΔU, $\Delta U = -1.5W$ (red), $\Delta U = -1.0W$ (green), and $\Delta U = -0.5W$ (blue). The values of $E_{f,\alpha}$ and V are the same as in Fig. 2.2.

little change of the densities of states even when the deep energy bound states form. This indicates that both the virtual bound state and the deep-energy bound states are well localized on the scale of a lattice spacing. For $\mathbf{R} = (1, 1, 0)$, $\mathbf{R} = (1, 1, 1)$ and $\mathbf{R} = (2, 0, 0)$, the local densities of states are almost indistinguishable from the bulk one as can be seen in Fig. 2.6.

For d electrons, local densities of states can be calculated by similar equations like those for f electrons. On the impurity site, the spectral weight of the in-gap bound state contributed by d electrons is estimated to be $\frac{V^2}{V^2+E_{f,\alpha}^2+\frac{W^2}{6}}$ for moderately small values of ΔU. The sum rule for the in-gap state's spectral weight is saturated by the on-site d and the nearest neighbor f weights, in the limit of particle-hole symmetry

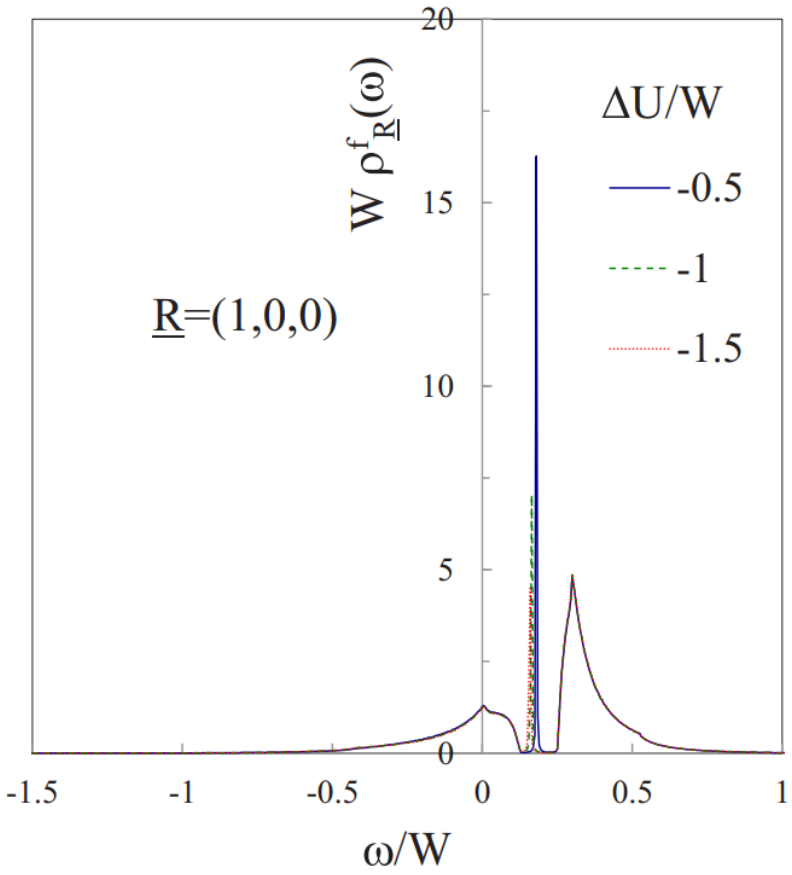

Figure 2.5: The dimensionless f-electron local densities of states of the site $\mathbf{R} = (1,0,0)$ for three values of ΔU, $\Delta U = -1.5W$ (red), $\Delta U = -1.0W$ (green), and $\Delta U = -0.5W$ (blue). The values of $E_{f,\alpha}$ and V are the same as in Fig. 2.2.

$E_{f,\alpha} \to 0$. As shown in Fig. 2.7, the continuous portion of the on-site d spectral densities of states shows the strong Fano antiresonance at $\omega \sim E_{f,\alpha} + \Delta U$. However, for $\mathbf{R} = (1,0,0)$, the strength of the antiresonance is diminished, shown in Fig. 2.8.

2.7 Discussion

In this hybridizing gap model of a Kondo insulator with impurities, we have shown that there are two kinds of bound states. In the first category, if the impurity potential exceeds a critical value comparable to the bandwidth, the bound states form, which

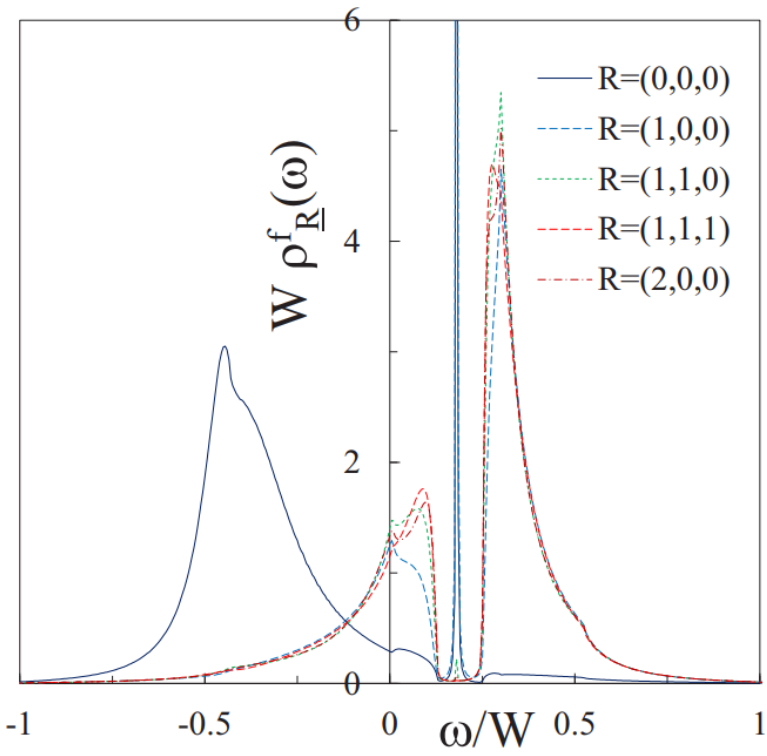

Figure 2.6: The dimensionless f-electron local densities of states of different sites $\mathbf{R}$ for $\Delta U = -0.5W$. The values of $E_{f,\alpha}$ and V are the same as in Fig. 2.2.

are split off from the upper (lower) edge of the conduction (valence) band. These bound states are very localized. For values of the impurity potential smaller than the critical value, the states merge with the continuous portions of the density of states and form broadened virtual bound states. For the second type of bound states, they form within the gap and can occur at extremely small values of the impurity potential, which can be significantly smaller than the hybridization gap. It means that this kind of system is extremely sensitive to small imperfections. It is also shown that these in-gap bound states are extended to neighboring atoms, which contrasts with the first kind of impurity state. Additionally, because these in-gap states are not localized, they are comparable to metallic surface states supported by the topological insulators. They should behave similarly in transport experiments. However, they are distinct

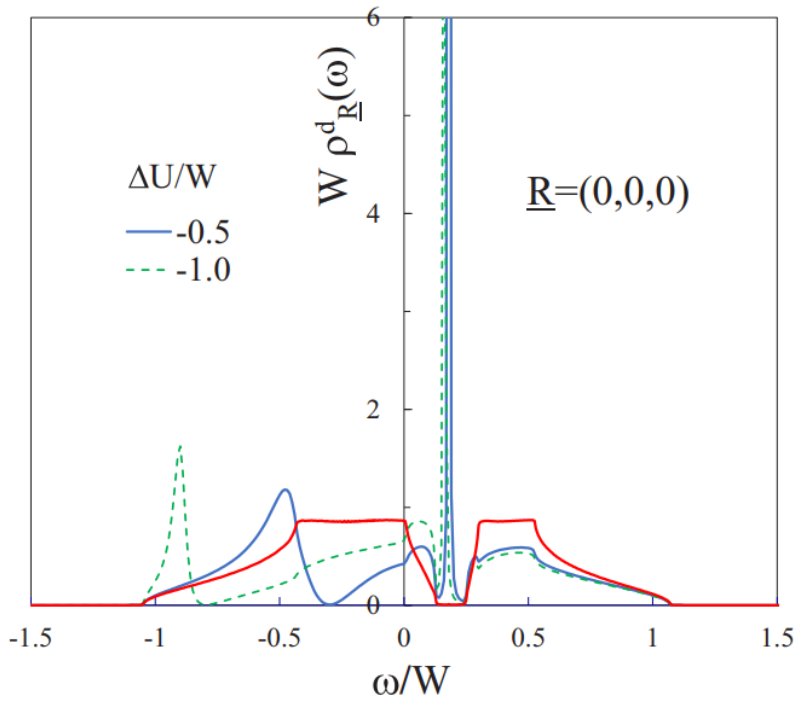

Figure 2.7: The dimensionless d-electron local densities of states of the impurity site for $\Delta U = -0.5W$ (blue) and $\Delta U = -1.0W$ (green) and the bulk d-electron density of states (red). The values of $E_{f,\alpha}$ and V are the same as in Fig. 2.3.

from each other in at least two ways. The first one is that for topological surface states, they should have an odd number of Dirac points which can be characterized by angle-resolved photoemission spectroscopy (ARPES), which are absent in in-gap impurity states. Secondly, for the impurity states, they should have a dispersionless band structure, while the topological surface states are linearly momentum dependent.

Since the proposal of the topological Kondo insulators, there are numerous experiments on one of the most promising candidate, SmB_6. Since the discovery of SmB_6, it has shown unusual properties one after one. It is a good conductor in room temperature but its resistivity increases up to 10^5 times at low temperature. In addition, unlike normal insulators, it has universal saturated resistivity below around 4K. However, it has only recently been unambiguously shown that the saturated re-

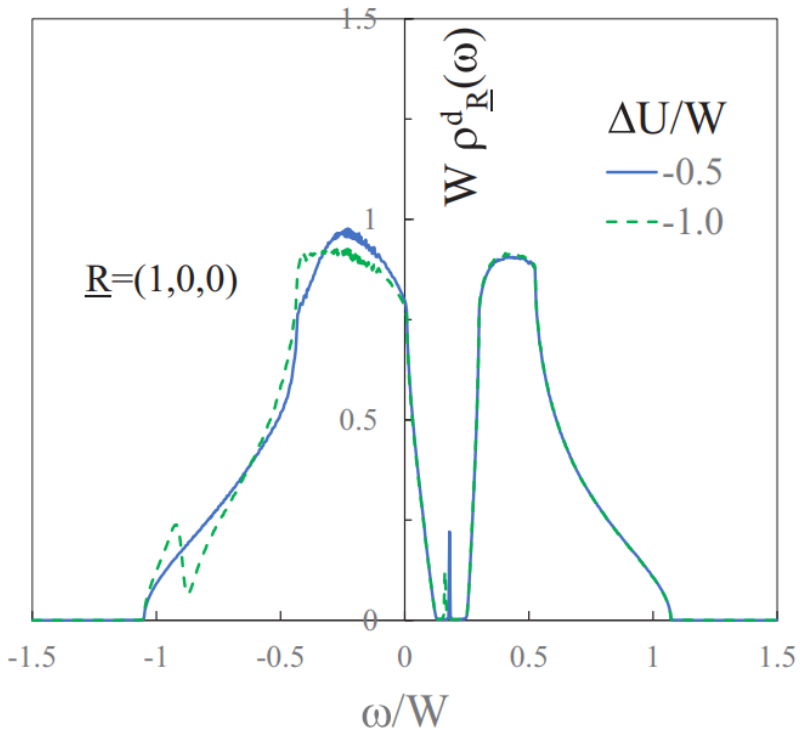

Figure 2.8: The dimensionless d-electron local densities of states of the site $\mathbf{R} = (1, 0, 0)$ for $\Delta U = -0.5W$ (blue) and $\Delta U = -1.0W$ (green). The values of $E_{f,\alpha}$ and V are the same as in Fig. 2.3.

sistivity comes from the surface in some transport experiments [10, 11], while the bulk resistivity increases when the temperature is lowered below 4k. Combined with some ARPES experiment results [12], SmB_6 is expected to be the first discovered topological Kondo insulator. However, some ARPES experiments indicate that the surface states of SmB_6 are topologically trivial [13]. In our model, we show that the surface states can come from impurities since surfaces are nature defects where surface reconstruction is inevitable. Such conductive surface states should persist even SmB_6 is to be proven topologically trivial.

2.8 Summary

We have presented an impurity model applicable to topological Kondo insulators. There are two different types of impurity states, deep-bound impurity states and in-gap bound states, respectively. The in-gap bound states are extensive, making them behave similarly to topological surface states in transport experiments. It can be used to explain the conducting surface states of SmB_6 even if SmB_6 turns out not to be a topological insulator.

CHAPTER 3

ENHANCED SPIN-ORBIT COUPLING IN ITINERANT $5F$ METALS

Many-body interactions can lead to the enhancement of the spin-orbit coupling especially in materials of heavy elements which normally have strong spin-orbit coupling and strong Coulomb interaction. Here, we use the underscreened Anderson lattice model that was proposed to study uranium and plutonium compounds to analyze the possible spin-orbit coupling enhancement. By using a rotational invariant approximation, we show that Coulomb interactions induce off-diagonal correlations that enhance the components of the spin-orbit coupling. Even modest values of the Coulomb interaction U can enhance the spin-orbit coupling by factors of about 4 and have significant effects on the electronic spectrum, but the enhancements are most pronounced for systems that are on the verge of magnetic instability. The enhancement is anisotropic in crystals with non-cubic symmetries and can lead to giant magnetic anisotropies in paramagnetic states. The main part of this chapter has been published [14].

3.1 Introduction

Actinide materials exhibit many characteristics of strong electronic correlations and strong spin-orbit interaction, such as those found in uranium compounds. Unlike the $4f$ wave functions in the lanthanide series, the $5f$ wave functions are more extended and are more susceptible to environmental effects, such as crystal symmetry which, when combined with spin-orbit coupling, lead to giant magnetic anisotropies. The giant anisotropies have even been observed in the cubic ferromagnetic uranium monochalcogenides [15] and in the magnetically ordered phases of tetragonal URu_2Si_2 [16, 17]. There is also evidence that the spin-orbit interaction is enhanced in the magnetically ordered phase of α-plutonium [18, 19]. These exceptionally large magnetic anisotropies persist in nonmagnetic states. Definitive measurements of the spin-orbit splitting in metallic compounds are lacking. Although there have been predictions of a spin-orbit splitting in the unoccupied portion of the $5f$ density of states in uranium and Pu compounds [20, 21, 22, 23], for the most part, the measured BIS spectra only show shoulders close to the main peak [24]. The absence of the predicted gaps can be attributed to the neglect of finite lifetimes due to inelastic scattering processes and thermal smearing, but it is found that the low-energy BIS structure is considerably different in different structures [25, 26, 27].

The underscreened Anderson model was formulated to distinguish the properties of the anomalous lanthanide compounds, such as those containing Ce or Yb, from the properties of actinide materials containing U, Np and Pu. The $4f$ orbitals of the lanthanide series are inner orbitals and usually the $4f$ electrons are highly localized and form magnetic moments. However, in the anomalous lanthanide materials, the $4f$ electrons delocalize through hybridization with the itinerant conduction band states and the local magnetic moments are quenched at low temperatures. This is frequently

described in terms of the Kondo effect, in which the $4f^1$ moments of Ce or the $4f^{13}$ moments of Yb are represented as $S = \frac{1}{2}$ moments which are fully compensated by the spin one-half moments of the conduction electrons. In the instances where the anomalous lanthanide materials order magnetically, the ordered magnetic moments are only fractions of a Bohr magneton and the ordering temperatures are of the order of 5 K. By contrast, in uranium compounds, the $5f$ electrons are considered to be in an admixture of $5f^2$ and $5f^3$ configurations but with quenched orbital angular momentum since the $5f$ electrons contribute to chemical bonding. The model was initially formulated to describe a $5f^2$ configuration, the electronic spins are aligned by the Hund's rule exchange interaction to yield $S = 1$. In this case, one may expect that the Kondo effect only partially compensates the local moments, and that the partially compensated moments will magnetically order at temperatures below the Kondo temperature. The underscreened Kondo model picture was first proposed to describe the uranium monochalcogenides [28], where transport measurements show logarithmic temperature variations over several decades of temperature [29] but which order ferromagnetically at relatively high temperatures, of the order of 100 K, and have ordered magnetic moments of the order of a Bohr magneton [15]. The underscreened Anderson lattice model represents an extension of the underscreened Kondo model, which recognizes the extended nature of the $5f$ electronic wave functions and incorporates the delocalization through direct f-f hopping as well as through the hybridization with the conduction bands.

Here we use the underscreened Anderson lattice model to investigate the interplay of Coulomb interactions and spin-orbit interactions, focusing on the effects of the crystalline anisotropy. We shall use a mean-field approximation to treat the electronic correlations, since the effect that we are describing relies on long-lived large amplitude correlations which extend throughout the structure, which soften and become static

when the material undergoes a transition to long-ranged magnetically ordered states. Within mean-field theory, for even modest Coulomb interaction strengths far below the critical value required to produce magnetic ordering, the Coulomb interaction can enhance the spin-orbit interaction by factors of the order of $2 \sim 4$. Furthermore, even though the bare spin-orbit coupling strength is the smallest energy scale in the model, when enhanced, it can have considerable effects on the spectrum of electronic excitations.

3.2 Model Hamiltonian

We use the underscreened Anderson lattice model [30, 31, 32, 33] to study a simple orthorhombic crystal system, where a set of A atoms are located at the $(0, 0, 0)$ sites and the second set of B atoms are located at $(\frac{a_x}{2}, \frac{a_y}{2}, \frac{a_z}{2})$ sites. The A atoms are set to contribute the itinerant conduction electrons, while the electrons in the B atom orbitals are more localized, subjected to spin-orbit coupling and strong electron-electron interactions. To simplify the calculations, we consider the orbitals of A atoms are non-degenerate and those of B atoms are triply degenerate. The Hamiltonian can be represented as the sum of three terms,

$$\hat{H} = \hat{H}_A + \hat{H}_B + \hat{H}_{AB}. \tag{3.1}$$

$\hat{H}_A$ describes the Hamiltonian for the conduction band

$$\hat{H}_A = \sum_{\mathbf{k},\sigma} \epsilon_A(\mathbf{k}) c^\dagger_{\mathbf{k},\sigma} c_{\mathbf{k},\sigma} \tag{3.2}$$

in which $c^{\dagger}_{\mathbf{k},\sigma}$ and $c_{\mathbf{k},\sigma}$, respectively, creates and annihilate an electron of Bloch wave vector $\mathbf{k}$ and spin σ. The dispersion relation is

$$\epsilon_A(k) = E_A + 2t_A(a_x)\cos k_x a_x + 2t_A(a_y)\cos k_y a_x + 2t_A(a_z)\cos k_z a_z. \tag{3.3}$$

$t_A(a_\alpha)$ is the corresponding Slater-Koster integral [34] and a_α is the corresponding lattice constant. Typical values of the conduction band width are of the order of 10 eV and are expected to be the largest energy scale of the model.

The Hamiltonian for the electrons in the orbitals of the B atoms are described by the sum of a tight-binding Hamiltonian $\hat{H}_0$, the spin-orbit coupling $\hat{H}_{S0}$, and the Coulomb interaction $\hat{H}_{int}$

$$\hat{H}_B = \hat{H}_0 + \hat{H}_{SO} + \hat{H}_{int}. \tag{3.4}$$

The tight-binding one is given by

$$\hat{H}_0 = \sum_{\mathbf{k},\alpha,\sigma} \epsilon_{B,\alpha}(\mathbf{k}) f^{\dagger}_{\mathbf{k},\alpha,\sigma} f_{\mathbf{k},\alpha,\sigma}, \tag{3.5}$$

where $\alpha = x, y, z$, and $f^{\dagger}_{\mathbf{k},\alpha,\sigma}$ and $f_{\mathbf{k},\alpha,\sigma}$ respectively create and annihilate an electron of the α orbitals of B atoms with spin σ. The dispersion relation is given by

$$\epsilon_{B,\alpha}(\mathbf{k}) = E_B + \sum_{\beta} 2\left(t_{B,\beta} + \delta_{\alpha,\beta}\Delta t_{B,\beta}\right)\cos k_\beta a_\beta, \tag{3.6}$$

where β runs over x, y, z. $t_{B,\beta}$ and $\Delta t_{B,\beta}$ are expressed in terms of the Slater–Koster integrals

$$t_{B,\beta} = t^{\pi}_{B,B}(a_\beta), \tag{3.7}$$

$$\Delta t_{B,\beta} = t^{\sigma}_{B,B}(a_\beta) - t^{\pi}_{B,B}(a_\beta). \tag{3.8}$$

The crystalline electric field splittings of the $5f$ states of the actinides are expected to be an order of magnitude smaller than the spin-orbit interaction [35], therefore they are not included in this study. In the atomic representation, the spin-orbit coupling for the f electrons of an isolated ion is isotropic and can be expressed as

$$\hat{H} = \frac{\lambda}{2} \sum_{i,m,\sigma} \left(\sigma m f^{\dagger}_{m,\sigma} f_{m,\sigma} + \sqrt{l(l+1) - m(m+1)} \left(f^{\dagger}_{m,\sigma} f_{m+1,\overline{\sigma}} + f^{\dagger}_{m+1,\overline{\sigma}} f_{m,\sigma} \right) \right), \tag{3.9}$$

where m denotes the z component of the atomic orbital angular momentum and $\overline{\sigma} = -\sigma$. Since the $5f$ states are modeled as triply degenerate in the localized limit, in the cubic harmonic Bloch representation, the spin–orbit interaction has the form

$$\begin{aligned} \hat{H}_{SO} =& \frac{\lambda_z}{2} \sum_{\mathbf{k},\sigma} i\sigma \left(f^{\dagger}_{\mathbf{k},y,\sigma} f_{\mathbf{k},x,\sigma} - f^{\dagger}_{\mathbf{k},x,\sigma} f_{\mathbf{k},y,\sigma} \right) - \frac{\lambda_y}{2} \sum_{\mathbf{k},\sigma} \sigma \left(f^{\dagger}_{\mathbf{k},z,\sigma} f_{\mathbf{k},x,\overline{\sigma}} + f^{\dagger}_{\mathbf{k},x,\overline{\sigma}} f_{\mathbf{k},z,\sigma} \right) \\ &+ \frac{\lambda_x}{2} \sum_{\mathbf{k},\sigma} i \left(f^{\dagger}_{\mathbf{k},z,\sigma} f_{\mathbf{k},y,\overline{\sigma}} - f^{\dagger}_{\mathbf{k},y,\overline{\sigma}} f_{\mathbf{k},z,\sigma} \right), \end{aligned} \tag{3.10}$$

where we have introduced different coupling strengths in anticipation of the result that the Coulomb enhancement will break the atomic symmetry. However, without enhancement, the interaction is isotropic, so $\lambda_\alpha = \lambda_0$ for all α. The value of the atomic spin-orbit coupling for uranium is $\lambda_0 = 0.25$ eV and increases to $\lambda_0 = 0.33$ eV for plutonium. This suggests that the atomic spin-orbit coupling should be the smallest relevant parameter in the Hamiltonian. The interaction between the quasi-localized electrons is denoted as $\hat{H}_{int}$. The interaction is represented by on-site Coulomb interaction U and the Hund's rule interaction J between the electrons in an atomic shell. The atomic interactions U and J should depend on the pair of orbital quantum numbers, however we neglect this dependence but instead require that the interaction be invariant under both spin and orbital rotations [36, 37, 38]. The explicit expression

is

$$\begin{aligned}\hat{H}_{int} =& \frac{1}{2}\sum_{i,\alpha,\beta,\sigma} U\hat{n}_{i,\alpha,\sigma}\hat{n}_{i,\beta,\bar{\sigma}} + \frac{1}{2}\sum_{i,\alpha\neq\beta,\sigma}(U-J)\hat{n}_{i,\alpha,\sigma}\hat{n}_{i,\beta,\sigma} \\ & - \sum_{i,\alpha\neq\beta,\sigma} J f^{\dagger}_{i,\alpha,\sigma} f_{i,\alpha,\bar{\sigma}} f^{\dagger}_{i,\beta,\bar{\sigma}} f_{i,\beta,\sigma} + \frac{1}{2}\sum_{i,\alpha,\sigma} J\hat{n}_{i,\alpha,\sigma}\hat{n}_{i,\alpha,\bar{\sigma}},\end{aligned} \tag{3.11}$$

where α and β run over x, y, z. Thus, the strength of the intra-orbital Coulomb interaction, (i.e., $\alpha = \beta$) is given by $U' = U + J$ and, therefore, is distinct from the inter-orbital interaction U.

The hybridization term that couples the A and B orbitals has the form

$$\hat{H}_{AB} = \sum_{\mathbf{k},\alpha,\sigma} iV_{\alpha}(\mathbf{k})\left(c^{\dagger}_{\mathbf{k},\sigma} f_{\mathbf{k},\alpha,\sigma} - f^{\dagger}_{\mathbf{k},\alpha,\sigma} c_{\mathbf{k},\sigma}\right), \tag{3.12}$$

where the k-dependent hybridization matrix elements are given by

$$V_{\alpha}(\mathbf{k}) = 8V_{AB}\frac{a_{\alpha}}{\sqrt{\sum_{\beta} a^2_{\beta}}}\sin\frac{k_{\alpha}a_{\alpha}}{2}\prod_{\gamma\neq\alpha}\left(\cos\frac{k_{\gamma}a_{\gamma}}{2}\right), \tag{3.13}$$

in which V_{AB} is the Slater-Koster parameter $t^{\sigma}_{A,B}(R)$ where R is the distance between the atoms

$$R^2 = \sum_{\beta} a^2_{\beta}. \tag{3.14}$$

The hybridization is primarily responsible for the width of the $5f$ band. It describes a coupling between the quasi-localized $5f$ orbitals and the extensive conduction electrons that are located on the nearest neighbor atoms. Although the direct $5f - 5f$ tight-binding matrix elements delocalize the $5f$ states, their contribution to the $5f$ band width is much smaller than the hybridization since they couple quasi-localized $5f$ states of next nearest neighboring atoms. It is expected that the hybridization may vary dramatically from compound to compound, since the Slater-Koster inte-

grals exhibit both a node structure described by a Slater-Koster polynomial and have an envelope that decays exponentially with atomic separation. The generic form of

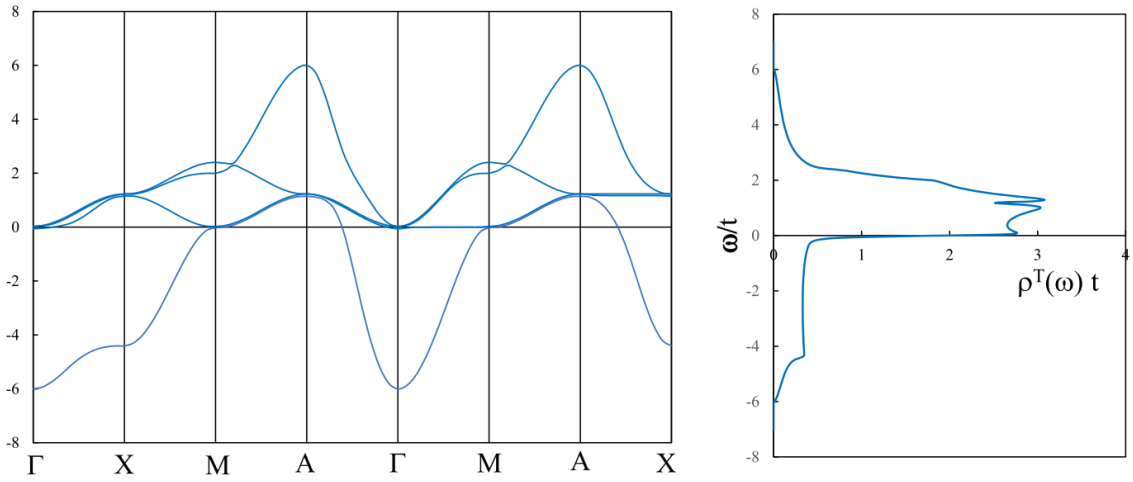

Figure 3.1: The generic form of the dispersion relations for the non-interacting model (left) and the dimensionless total density of states $\rho^T(\omega)t$ (right) for the underscreened Anderson model with cubic symmetry.

the dispersion relations for the non-interacting model is shown in Fig. 3.1. The figure shows that at the Γ and A points of the Brillouin zone, the degeneracy of the $5f$ bands is lifted and exhibits the same spin-orbit splitting as the atomic states. Furthermore, the spin-orbit coupling lifts the degeneracy of the $5f$ bands at the van Hove singularity of the density of states.

3.3 Mean-field Approximation

The Coulomb interactions are treated in the mean-field approximation, in which the off-diagonal correlations are included in a rotational invariant manner [39, 40]. The energy level is shifted due to the Coulomb interactions by

$$\Delta E_{B,\alpha,\sigma} = U'\overline{n}_{i,\alpha,\overline{\sigma}} + \sum_{\beta\neq\alpha}\left(U\overline{n}_{i,\beta,\overline{\sigma}} + (U-J)\overline{n}_{i,\beta,\sigma}\right), \tag{3.15}$$

where i is the site index. In the absence of spontaneous time-reversal symmetry breaking, the expectation values of the occupation numbers are spin-independent

$$\overline{n}_{i,\alpha,\sigma} = \overline{n}_{i,\alpha,\overline{\sigma}}. \tag{3.16}$$

The renormalized dispersion relations of the f sub-bands are denoted by

$$\epsilon_{B,\alpha,\sigma}(\mathbf{k}) = \epsilon_{B,\alpha}(\mathbf{k}) + \Delta E_{B,\alpha,\sigma}. \tag{3.17}$$

As shown in reference, the spin-orbit coupling induces off-diagonal Coulomb correlations in the mean-field Hamiltonian of the form

$$\hat{H}^{OD}_{MF} = \sum_{i,\alpha,\sigma,\alpha',\sigma'} \Phi^{\alpha,\alpha'}_{\sigma,\sigma'} f^{\dagger}_{i,\alpha,\sigma} f_{i,\alpha',\sigma'} \tag{3.18}$$

which, in the absence of spontaneous symmetry breaking, are restricted to have the same form as the set of terms that occur in the spin-orbit interaction shown in Eq. 3.10. The independent values of the off-diagonal elements are given by

$$\Phi^{x,y}_{\sigma,\sigma} = -\left(U - J\right) \langle f^{\dagger}_{i,y,\sigma} f_{i,x,\sigma} \rangle + J \langle f^{\dagger}_{i,y,\overline{\sigma}} f_{i,x,\overline{\sigma}} \rangle , \tag{3.19}$$

$$\Phi^{x,z}_{\sigma,\overline{\sigma}} = -\,U \langle f^{\dagger}_{i,z,\overline{\sigma}} f_{i,x,\sigma} \rangle , \tag{3.20}$$

$$\Phi^{y,z}_{\overline{\sigma},\sigma} = -\,U \langle f^{\dagger}_{i,z,\sigma} f_{i,y,\overline{\sigma}} \rangle . \tag{3.21}$$

As will be seen later, the off-diagonal non-spin-flip correlations are odd functions of σ, so that the terms proportional to J cancel. This results in an enhancement of the

spin-orbit coupling that can be expressed as

$$-i\sigma\frac{\lambda_z}{2} = -i\sigma\frac{\lambda_0}{2} - U\left\langle f^\dagger_{i,y,\sigma} f_{i,x,\sigma}\right\rangle, \tag{3.22}$$

$$-\sigma\frac{\lambda_y}{2} = -\sigma\frac{\lambda_0}{2} - U\left\langle f^\dagger_{i,z,\sigma} f_{i,x,\bar{\sigma}}\right\rangle, \tag{3.23}$$

$$-i\frac{\lambda_x}{2} = -i\frac{\lambda_0}{2} - U\left\langle f^\dagger_{i,z,\sigma} f_{i,y,\bar{\sigma}}\right\rangle. \tag{3.24}$$

Hence, the mean-field approximation reduces to an effective single-particle theory in which the spin–orbit coupling is modified. This modification should be viewed in terms of the additivity of the scattering amplitudes from Coulomb and spin-orbit scattering. Although the change in the spin-orbit coupling is proportional to the direct Coulomb interaction U, its magnitude is proportional to the off-diagonal correlation, which is nominally proportional to the spin-orbit coupling. Therefore, scattering mechanisms can act coherently to enhance the spin-orbit coupling. The mean-field Hamiltonian can be written as

$$\hat{H}_{MF} = \sum_k \psi^\dagger_{\mathbf{k}} \mathcal{H}_{\mathbf{k}} \psi_{\mathbf{k}}, \tag{3.25}$$

where $\psi^\dagger_{\mathbf{k}}$ is defined by

$$\psi^\dagger_{\mathbf{k}} = \begin{pmatrix} f^\dagger_{\mathbf{k},x,\uparrow} & f^\dagger_{\mathbf{k},y,\uparrow} & f^\dagger_{\mathbf{k},z,\uparrow} & f^\dagger_{\mathbf{k},x,\downarrow} & f^\dagger_{\mathbf{k},y,\downarrow} & f^\dagger_{\mathbf{k},z,\downarrow} & c^\dagger_{\mathbf{k},\uparrow} & c^\dagger_{\mathbf{k},\downarrow} \end{pmatrix}. \tag{3.26}$$

The Hamiltonian matrix is

$$\mathcal{H}_{\mathbf{k}} = \begin{pmatrix} \epsilon_{B,x,\uparrow} & -i\frac{\lambda_z}{2} & 0 & 0 & 0 & \frac{\lambda_y}{2} & -iV_x & 0 \\ -i\frac{\lambda_z}{2} & \epsilon_{B,y,\uparrow} & 0 & 0 & 0 & -i\frac{\lambda_x}{2} & -iV_y & 0 \\ 0 & 0 & \epsilon_{B,z,\uparrow} & -\frac{\lambda_y}{2} & i\frac{\lambda_x}{2} & 0 & -iV_z & 0 \\ 0 & 0 & -\frac{\lambda_y}{2} & \epsilon_{B,x,\downarrow} & i\frac{\lambda_z}{2} & 0 & 0 & -iV_x \\ 0 & 0 & -i\frac{\lambda_x}{2} & -i\frac{\lambda_z}{2} & \epsilon_{B,y,\downarrow} & 0 & 0 & -iV_y \\ \frac{\lambda_y}{2} & i\frac{\lambda_x}{2} & 0 & 0 & 0 & \epsilon_{B,z,\downarrow} & 0 & -iV_z \\ iV_x & iV_y & iV_z & 0 & 0 & 0 & \epsilon_{A,\uparrow} & 0 \\ 0 & 0 & 0 & iV_x & iV_y & iV_z & 0 & \epsilon_{A,\downarrow} \end{pmatrix}. \tag{3.27}$$

The single-electron Green's functions are defined as

$$G_{\alpha,\sigma,\alpha',\sigma'}(t,\mathbf{k}) = -i\left\langle \hat{T} a_{\mathbf{k},\alpha,\sigma}(t) a^{\dagger}_{\mathbf{k},\alpha',\sigma'}(0)\right\rangle. \tag{3.28}$$

The Green's functions satisfy the equations of motion

$$i\frac{\partial}{\partial t} G_{\alpha,\sigma,\alpha',\sigma'}(t,\mathbf{k}) = \delta(t)\delta_{\alpha,\alpha'}\delta_{\sigma,\sigma'} - i\left\langle \hat{T}[a_{\mathbf{k},\alpha,\sigma}(t), \hat{H}_{MF}] a^{\dagger}_{\mathbf{k},\alpha',\sigma'}(0)\right\rangle. \tag{3.29}$$

The Fourier transform of the Green's function is

$$G_{\alpha,\sigma,\alpha',\sigma'}(\omega,\mathbf{k}) = \int_{-\infty}^{\infty} dt \exp(i\omega t) G_{\alpha,\sigma,\alpha',\sigma'}(t,\mathbf{k}). \tag{3.30}$$

On Fourier transforming the equations of motion, one finds the Green's functions satisfy the set of coupled algebraic equations

$$\sum_{\alpha'',\sigma''} \left(\omega\hat{I} - \mathcal{H}_{\mathbf{k}}\right)_{\alpha,\sigma,\alpha'',\sigma''} G_{\alpha'',\sigma'',\alpha',\sigma'}(\omega,\mathbf{k}) = \delta_{\alpha,\alpha'}\delta_{\sigma,\sigma'}. \tag{3.31}$$

The Green's functions are found by multiplying by the inverse matrix

$$\left(\omega\hat{I} - \mathcal{H}_{\mathbf{k}}\right)^{-1}. \tag{3.32}$$

The inverse of the matrix is given by the transpose of the matrix of cofactors, divided by a determinant, $D_8(\omega, \mathbf{k})$. The determinant is an eight-order polynomial whose zero's determine the electronic dispersion relations. Since the system has been assumed to be time-reversal invariant and the structure is of inversion symmetry, Kramers theorem holds. Therefore, the dispersion relations are doubly-degenerate and the determinant can be factorized into two identical quartic polynomials

$$D_8(\omega, \mathbf{k}) = D_4(\omega, \mathbf{k})^2. \tag{3.33}$$

The two decoupled sets of states should be labeled by a pseudo-spin index, however, we shall omit this index and reserve the role of the two-fold index for spin and for convenience we let $\epsilon_{B,x} = \epsilon_x$, $\epsilon_{B,y} = \epsilon_y$, $\epsilon_{B,z} = \epsilon_z$, $\epsilon_A = \epsilon_a$. The diagonal Green's functions for the correlated sub-bands can be reduced to

$$G_{x,x}(\omega, \mathbf{k}) = \Bigg((\omega - \epsilon_y)(\omega - \epsilon_z)(\omega - \epsilon_a) - V_y^2(\omega - \epsilon_z) - V_z^2(\omega - \epsilon_y) - \frac{\lambda_x^2}{4}(\omega - \epsilon_a) \Bigg) / D_4(\omega, \mathbf{k}) \tag{3.34}$$

and

$$G_{z,z}(\omega, \mathbf{k}) = \Bigg((\omega - \epsilon_x)(\omega - \epsilon_y)(\omega - \epsilon_a) - V_x^2(\omega - \epsilon_y) - V_y^2(\omega - \epsilon_x) - \frac{\lambda_z^2}{4}(\omega_a - \epsilon) \Bigg) / D_4(\omega, \mathbf{k}). \tag{3.35}$$

The diagonal conduction band Green's function is given by

$$G_{a,a}(\omega,\mathbf{k}) = \left((\omega-\epsilon_x)(\omega-\epsilon_y)(\omega-\epsilon_z) + \frac{\lambda_x\lambda_y\lambda_z}{4} - \sum_{\alpha=x,y,z}\frac{\lambda_\alpha^2}{4}(\omega-\epsilon_\alpha)\right) /D_4(\omega,\mathbf{k}). \tag{3.36}$$

The non-spin-flip, off-diagonal, Green's function is given by

$$G_{x,\sigma,y,\sigma}(\omega,\mathbf{k}) = -i\sigma\left(\frac{\lambda_z}{2}\left((\omega-\epsilon_z)(\omega-\epsilon_a) - V_z^2\right) - \frac{\lambda_x\lambda_y}{4}(\omega-\epsilon_a)\right) /D_4(\omega,\mathbf{k}) + \frac{(\omega-\epsilon_z)V_xV_y}{D_4(\omega,\mathbf{k})}. \tag{3.37}$$

Since the non-spin-flip off-diagonal Green's function is proportional to σ, the off-diagonal equal-spin correlation in equation is also proportional to σ which produces a many-body enhancement of λ_z. The off-diagonal spin-flip Green's functions are given by

$$G_{z,\sigma,x,\overline{\sigma}}(\omega,\mathbf{k}) = -\sigma\left(\frac{\lambda_y}{2}\left((\omega-\epsilon_y)(\omega-\epsilon_a) - V_y^2\right) - \frac{\lambda_z\lambda_x}{4}(\omega-\epsilon_a)\right) /D_4(\omega,\mathbf{k}) + i\sigma\frac{\lambda_x}{2}\frac{V_xV_y}{D_4(\omega,\mathbf{k})} \tag{3.38}$$

and

$$G_{y,\overline{\sigma},z,\sigma}(\omega,\mathbf{k}) = -i\left(\frac{\lambda_x}{2}\left((\omega-\epsilon_x)(\omega-\epsilon_a) - V_x^2\right) - \frac{\lambda_y\lambda_z}{4}(\omega-\epsilon_a)\right) /D_4(\omega,\mathbf{k}) + \sigma\frac{\lambda_y}{2}\frac{V_xV_y}{D_4(\omega,\mathbf{k})}. \tag{3.39}$$

The off-diagonal expectation values are obtained by integration over ω and summation over k. Since V_x and V_y are odd functions of k_x and k_y respectively and $D_4(\omega,\mathbf{k})$ is an even function of $\mathbf{k}$, the terms nominally proportional to the product of V_xV_y are proportional to $\sin k_xa_x \sin k_ya_y$. Due to the inversion symmetry, the terms proportional

to $V_x V_y$ cancel after summation over $\mathbf{k}$. Thus, on comparing with Eq. 3.10, one sees that the off-diagonal correlations have the same forms as the respective components of the spin-orbit interaction. To summarize, both the spin-orbit interaction and the direct Coulomb interaction produce spin-flip inter-orbital scattering processes which have the same symmetries, so both interactions can act cooperatively to amplify the spin-orbit interaction.

The normalized partial densities of states $\rho^{\alpha}(\omega)$, per spin, are calculated from the diagonal Green's functions as

$$\rho^{\alpha}(\omega) = -\lim_{\eta \to 0^+} \frac{1}{\pi} \frac{1}{N} \sum_{\mathbf{k}} \operatorname{Im} G_{\alpha,\alpha}(\omega + i\eta, \mathbf{k}). \tag{3.40}$$

The total density of states can also be projected onto the eigenstates of $j = l \pm \frac{1}{2}$. The projected density of states is composed of an isotropic diagonal piece and an anisotropic piece

$$\rho_{l\pm\frac{1}{2}}(\omega) = -\lim_{\eta \to 0^+} \frac{1}{(2l+1)N} \sum_{\mathbf{k}} \operatorname{Im} \left(\sum_{\alpha,\sigma} G_{\alpha,\sigma}(\omega + i\eta, \mathbf{k}) \pm \Delta G(\omega + i\eta, \mathbf{k}) \right), \tag{3.41}$$

where the deviation from the average density of states, ΔG, is expressed in terms of the off-diagonal Green's functions

$$\Delta G(\omega, \mathbf{k}) = 2 \sum_{\sigma} \left(i\sigma G_{x,\sigma,y,\sigma}(\omega, \mathbf{k}) - \sigma G_{z,\sigma,x,\overline{\sigma}}(\omega, \mathbf{k}) - i G_{y,\overline{\sigma},z,\sigma}(\omega, \mathbf{k}) \right). \tag{3.42}$$

For tetragonal symmetry, the components of the spin-orbit coupling induced by

the Coulomb interaction can be expressed as

$$\Delta\lambda_z = U\chi_z^{(1)}(\mu)\lambda_z + U\chi_z^{(2)}(\mu)\lambda_x^2, \tag{3.43}$$

$$\Delta\lambda_x = U\chi_x^{(1)}(\mu)\lambda_x + U\chi_z^{(2)}(\mu)\lambda_x\lambda_z. \tag{3.44}$$

The quasi-linear response function $\chi^{(1)}(\mu)$ is positive and has a magnitude comparable to that of the sub-band density of states, and the bilinear susceptibility $\chi_z^{(2)}(\mu)$ is isotropic and changes sign when the $5f$ bands are more than approximately half-filled, as can be seen by examining the off-diagonal Green's function. The full self-consistency equations for the diagonal correlations are solved iteratively. Since our analysis is limited to the paramagnetic state, we shall restrict the values of U and J to be less than the critical values required to produce ferromagnetism. In the absence of spin-orbit coupling, the Stoner criterion becomes

$$\left(1 - (U+J)\rho^z(\mu)\right)\left(1 - (U+2J)\rho^x(\mu)\right) - 2J^2\rho^x(\mu)\rho^z(\mu) = 0 \tag{3.45}$$

which, for a cubic material, reduces to

$$(U+3J)\rho^\alpha(\mu) = 1. \tag{3.46}$$

The effect of the Hund's rule exchange is of aligning the electronic spins in the f-shell, thereby lending extra stability to the ferromagnetic state. The value of the Hund's rule exchange is set as $J = U/6$.

3.4 Results

The hopping parameters of the model will be chosen so as to be illustrative of what effects might be observable in uranium compounds. In atomic uranium, the spin-orbit coupling is expected to split the electronic states into a sixfold degenerate multiplet and an eightfold degenerate excited multiplet. Since uranium ions are expected to be in the $5f^3$ configuration, the states of the lower multiplet are approximately half-filled. Therefore, we shall focus our attention on the case where the model's lower spin-orbit multiplet is approximately half-filled and the conduction band is occupied by approximately one electron.

Typical values of the screened Coulomb interaction for uranium are in the range $1.2 < U < 3$ eV [22, 41, 42, 43, 44], although values as large as 6 eV have been used to fit experimental data [45]. Estimates of U for plutonium are slightly higher and are in the range of $2.9 < U < 4$ eV [46]. The magnitudes of the Hund's rule exchange interactions for uranium and plutonium are not as highly screened and remain close to the atomic values, so typical estimates are in a much tighter range of $0.4 < J < 0.6$ eV. The magnitude of the atomic spin-orbit coupling for uranium is $\lambda_0 \sim 0.25$ eV while for plutonium the value is $\lambda_0 \sim 0.33$ eV [47, 48]. Typical conduction band widths are of the order of 10 eV, and the calculated and experimentally measured $5f$ band widths [25, 27] for the metallic actinides are of the order of 2 to 3 eV.

Since the tight-binding parameter is set at $t_{AA} = -t$, the nominal conduction band width is $12t$, to be consistent with the calculated [47] and experimentally [25, 27] observed band widths we consider $5f$ band widths in the range of $2t - 3t$. The atomic spin-orbit coupling is chosen to have the fixed value of $\lambda_0 = 0.24t$ which, in the absence of an enhancement, would lead to an atomic spin-orbit splitting of $(2l + 1)\lambda_0/2 = 0.36t$. However, as we shall show, a direct Coulomb interaction U

of the order of $1 \sim 2t$, although insufficient to produce magnetic order, can enhance the spin-orbit interaction by a factor of $2 \sim 4$ while at a quantum critical point the enhancement can increase to the value of ~ 5.

Here we shall search for systematic dependence of the strength of the spin-orbit interaction on the c/a ratio and the hybridization strength V since the other parameters U, J and λ_0 are not expected to vary appreciably for the light actinide materials. First, we shall examine the enhancement of the spin-orbit coupling with U for high-symmetry cubic materials and then use fixed values of the atomic spin–orbit coupling U, J and λ_0, to study the spin-orbit correlations and typical forms of the density of states to facilitate comparison with the subsequent calculations of low-symmetry tetragonal materials.

3.4.1 Cubic Materials

Cubic materials are quite unusual in compounds containing elements in the early actinide series, since the itinerant nature of the $5f$ electrons causes them to adopt low-symmetry open structures [49]. Nevertheless, the uranium monochalcogenides and monopnictides adopt high-symmetry rock-salt structures due to the large strength of the $5f$-p hybridization and its directional dependence. The $5f$ tight-binding parameters are chosen as $t^{\sigma}_{B,B} = 0.3t$ and $t^{\pi}_{B,B} = -0.3t$.

The spin-orbit coupling enhancement λ/λ_0 factor is shown in Fig. 3.2 as a function of the Coulomb interaction for various values of U, for a value of the occupation number of the f electrons fixed at $n_f = 1.13$, $J = U/6$ and various values of the hybridization V. The values are calculated for a paramagnetic state, which occurs for U values below a critical value that is determined by the $5f$ sub-band densities of states at the Fermi energy. As seen in Fig. 3, the $5f$ band width increases with hybridization since it delocalizes the $5f$ electrons. As a consequence, the critical value

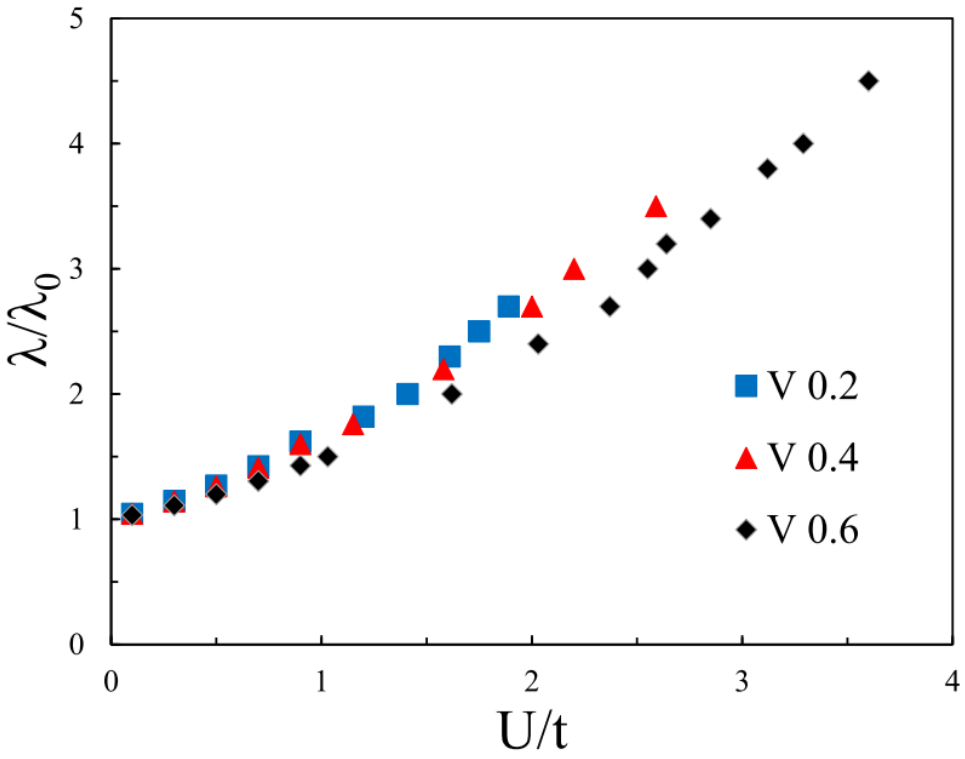

Figure 3.2: The enhancement factor for the spin orbit coupling, λ/λ_0, for the paramagnetic state, as a function of U/t for various values of the hybridization V. For $V/t = 0.2$ the paramagnetic state becomes unstable to ferromagnetism around $U/t = 1.89$, for $V/t = 0.4$ the paramagnetic state becomes unstable near $U/t = 2.59$. The largest enhancement factors are found close to the quantum critical points.

of U also increases as V increases. It is seen that the largest values of the enhancement occur close to the quantum critical point, and that the maximum enhancement is found for the larger values of the hybridization.

The partial densities of states of $5f$ band in a cubic basis, x, and the conduction band, c, are shown in Fig. 3.3 for various ratios of the hybridization strengths $V = t^{\sigma}_{AB}(R)$ to the interatomic hopping strength t. The mixing between the $5f$ and the conduction band states is most clearly seen in the anti-resonance in the conduction band density of states, c. Increasing hybridization is seen to have the effect of delocalizing the $5f$ electrons by a modest increase in the extent of the tails of

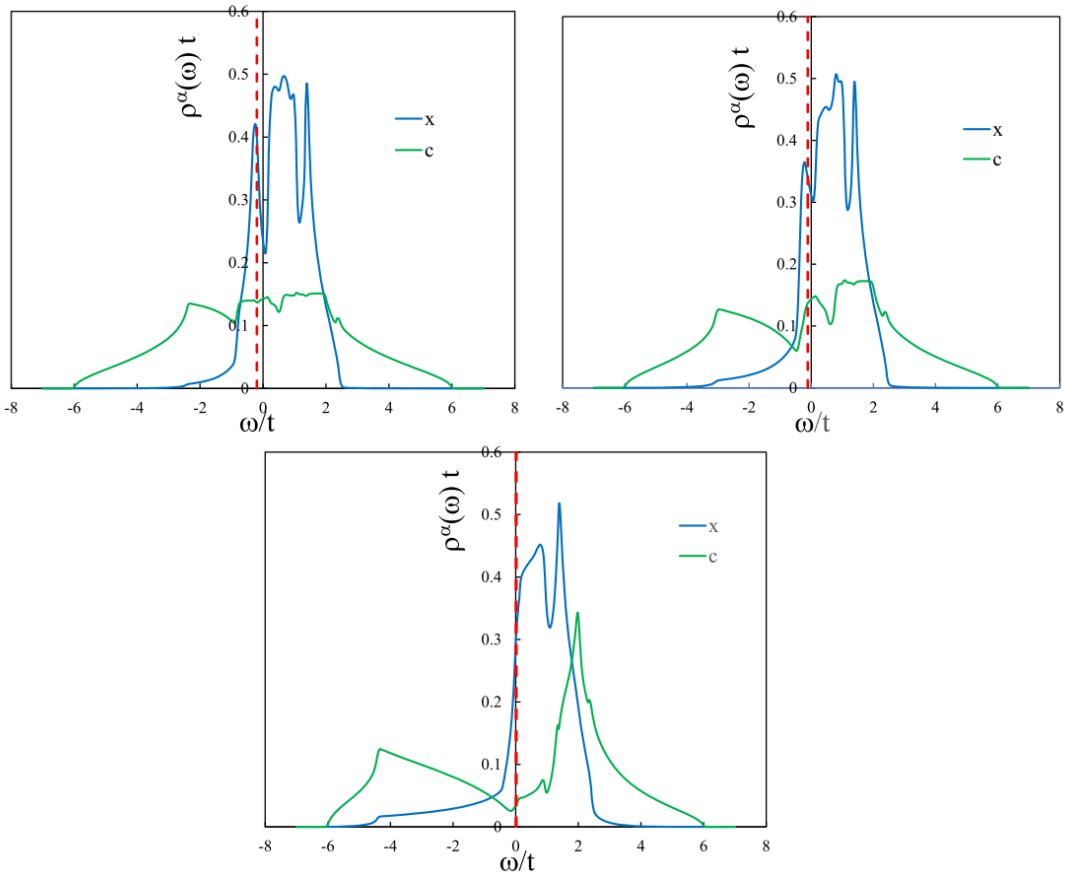

Figure 3.3: The decomposition of the dimensionless density of states in terms of the partial densities of states $\rho^{\alpha}(\omega)t$ in a cubic basis, per spin, for $V = 0.15t$ (top left), $V = 0.3t$ (top right), and $V = 0.6t$ (bottom). The spin-orbit coupling has been enhanced by a factor of 1.5.

the $5f$ band. It is also evident that the bare atomic spin-orbit interaction produces two pseudo-gaps in the density of states located at energies above the Fermi energy, which become less significant with increasing hybridization. Similar spin–orbit splittings have been previously predicted in electronic structure calculations for uranium systems [21, 22].

For the parameters shown in Fig. 3.3, the total density of the states at the Fermi-energy is approximately 1.86-2.68 states per t, and the $5f$ sub-band densities

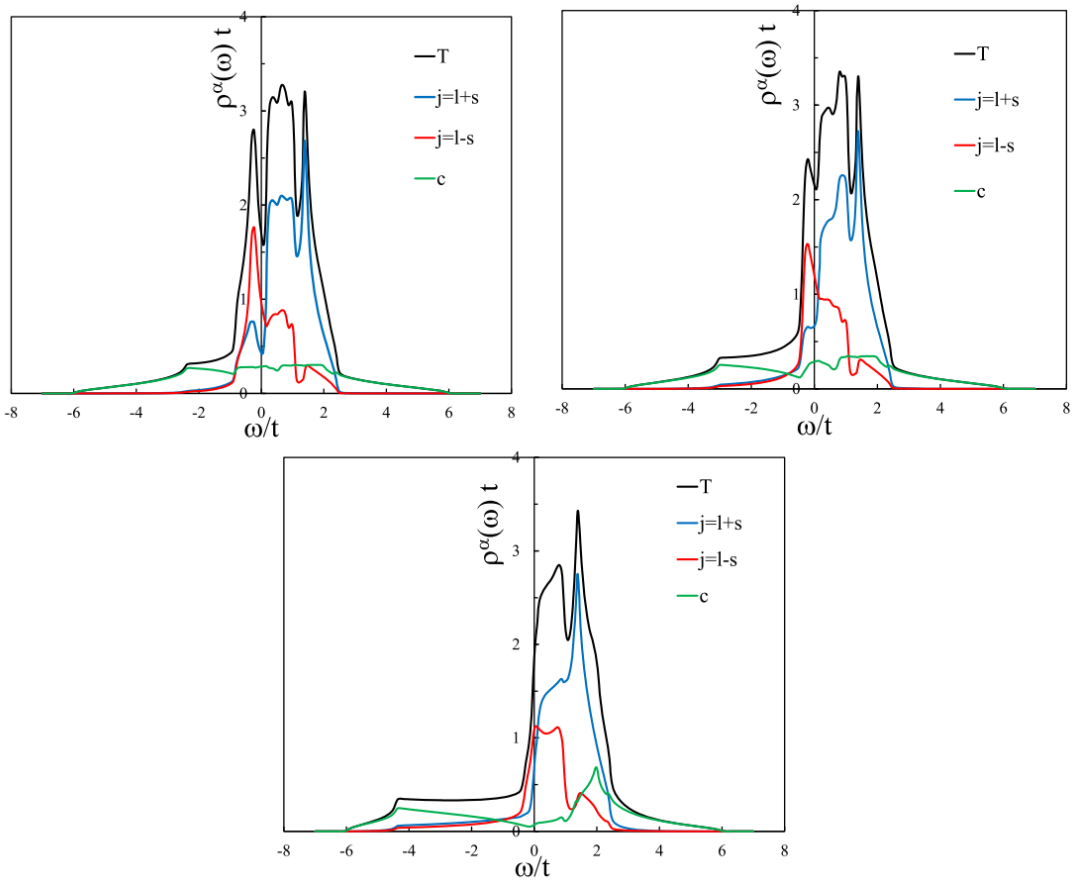

Figure 3.4: The dimensionless total density of states $\rho^T(\omega)t$ and its projections onto eigenstates of $j = l \pm s$ and on the conduction band state c for $V = 0.15t$ (top left), $V = 0.3t$ (top right), and $V = 0.6t$ (bottom).

of states are of the order of 0.31-0.40 states per t. The lower peak in the density of states corresponds to a $5f$ electron occupation number of about 1, and the minimum just above the Fermi energy corresponds to an integrated $5f$ spectral weight of about 1.6. This latter number may be compared with the degeneracy of 2 associated with the lowest atomic multiplet of a fully-gapped atom. The energy separation of the peaks above and below both gaps correspond to $3\lambda_0$. The j projected $5f$ and conduction band densities of states are shown in Fig. 3.4 for different values of the hybridization strength. For small values of the hybridization, the hopping is seen to result in a significant mixing between the different j character, as is expected since

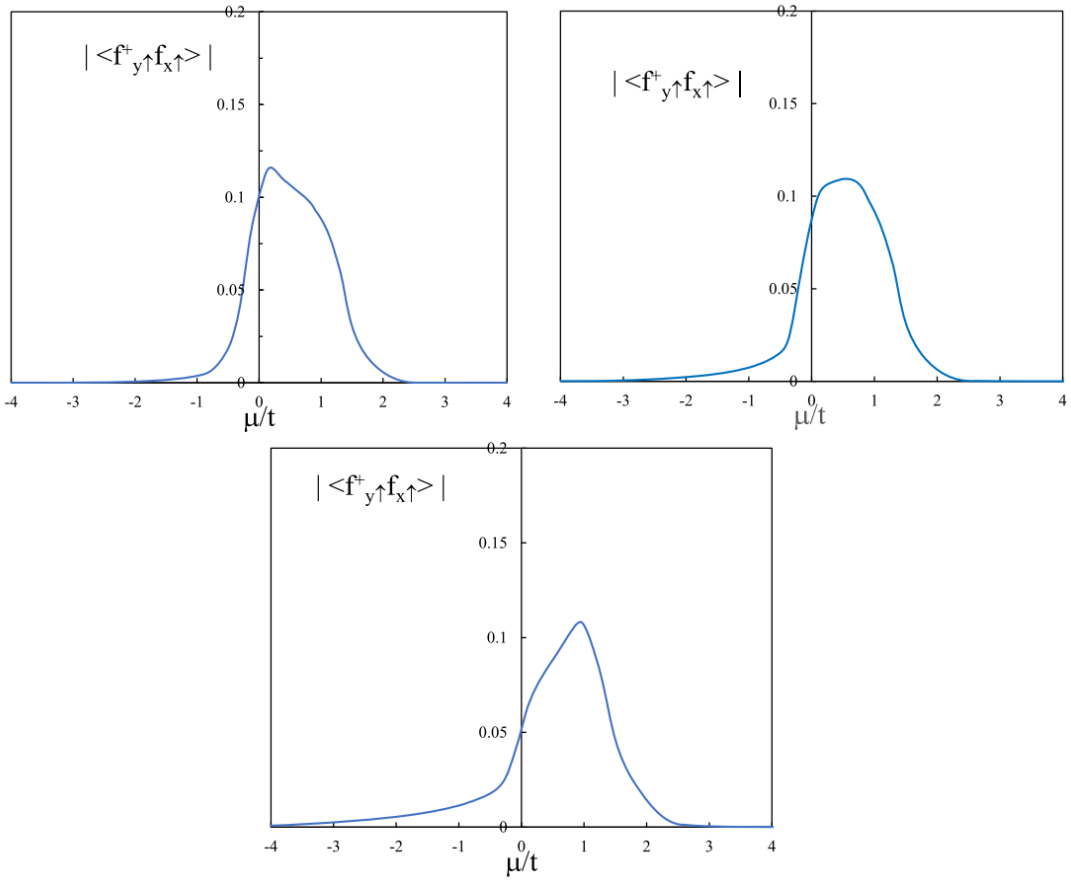

Figure 3.5: The magnitude of the off-diagonal correlation $\langle f^{\dagger}_{y,\uparrow} f_{x,\uparrow} \rangle$ as a function of μ/t calculated for the fixed sub-band occupation numbers found for $n_f = 1.13$ with $V = 0.15t$, $U = 0.9t$ (top left), $V = 0.3t$, $U = 0.9t$ (top right), and $V = 0.6t$, $U = 1.1t$ (bottom).

the interatomic hopping quenches the orbital angular momentum. The mixing ratios show jumps toward the 'atomic' values for narrow energy intervals at energies which correspond to the positions of the spin-orbit gaps. The peaked nature of the mixing indicates that the spin-orbit coupling is resonant at energies for which the branches of the electronic dispersion relations are nearly degenerate. Even though the first pseudogap in the spectrum is no longer apparent for $V = 0.6t$, the mixing ratio is still exhibiting a resonance-like energy-dependence in the region of the spin-orbit gap where it attains a peak value of around 3. The off-diagonal spin-orbit correlations

are calculated self-consistently from the off-diagonal Green's functions integrated up to μ. To enable comparison with the density of states in Fig. 3.3 and 3.4, we solve for the off-diagonal correlations as a function of μ/t but use the $5f$ band occupation numbers fixed by the self-consistent calculations with $n_f = 1.13$. The magnitudes of the results are shown in Fig. 3.5, where it is seen that the spin-orbit correlations are only appreciable for values of μ/t which correspond to partially occupied $5f$ density of states. For the cubic system, all the correlations are equivalent, as expected since the spin-orbit interaction is enhanced isotropically. The correlations are a dimensionless measure of the integrated spin-orbit mixing of the characters of the sub-bands and have a maximum value of unity. The magnitude of the peak decreases slightly with increasing hybridization as it moves to higher energies, which is in accord with the increased value of U from $0.9t$ to $1.1t$ that is required to maintain a constant enhancement as the system progressively delocalizes.

The induced spin-orbit correlation can be expressed in terms of a quasi-nonlinear response

$$2|\langle f^{\dagger}_{y,\uparrow} f_{x,\uparrow}\rangle| = \chi^{(1)}(\mu)\lambda + \chi^{(2)}(\mu)\lambda^2. \tag{3.47}$$

The forms of the linear and bilinear components of the quasi-nonlinear susceptibility are calculated from nonlinear response theory, using the diagonal $5f$ occupation numbers fixed at $n_f = 1.13$, as in Fig. 3.5. The results are shown in Fig.3.6 for variable μ/t. At the self-consistent value of μ, , the spin orbit interaction is enhanced by a factor of 3 but the magnetic susceptibility is enhanced by a Stoner factor of 5.1 for $V = 0.6t$ and by a factor of 2.1 at $V = 0.75t$. Although the quasi-linear susceptibility does show a broad maximum as μ is varied, it does not follow the density of states. However, the linear susceptibility has the same order of magnitude as the $5f$ sub-band density of states at the Fermi energy while the bilinear susceptibility changes sign at

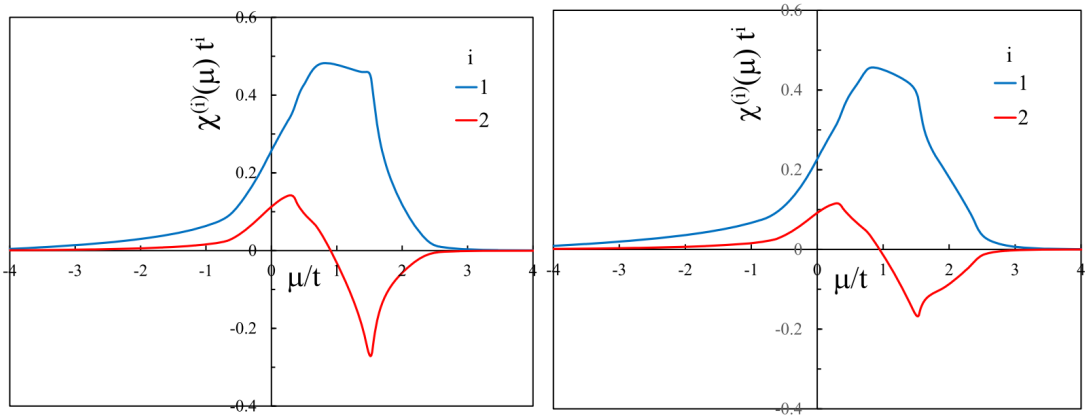

Figure 3.6: The forms of the dimensionless components of the nonlinear spin–orbit response, $\chi^{(i)}(\mu)t^i$ for $i = 1$ (blue) and for $i = 2$ (red), for $V = 0.6t$, $U = 2.69t$ (left) and $V = 0.75t$, $U = 1.93t$ (right).

half-filling of the $5f$ band. Since the spin-orbit interaction is increased by the product of the Coulomb interaction U and the off-diagonal correlations, for sufficiently small values of λ, the enhancement can be expressed in terms of the quasi-linear susceptibility

$$\lambda = \frac{\lambda_0}{1 - U\chi^{(1)}(\mu)}. \tag{3.48}$$

Since $\rho(\mu)$ has a magnitude slightly greater than the self-consistently calculated value of $\chi^{(1)}(\mu)$, large enhancements are expected for systems close to a ferromagnetic instability. For larger values of λ, the full self-consistency equation for λ must be used. Due to the increased importance of $\chi^{(2)}(\mu)$, giant enhancements are only found when the $5f$ band is less than half-filled and, due to the restriction of the analysis to paramagnetic states and the increasing spectral skew with increasing V, the largest enhancements are found for large values of V. Using the bare atomic value of the spin–orbit interaction as $\lambda_0 = 0.24t$, at the $V = 0.6t$ ferromagnetic quantum critical point, the spin-orbit interaction is enhanced by a factor of ~ 4.8, whereas for $V = 0.75t$ the enhancement is calculated as about 6 at the quantum critical point.

3.4.2 Tetragonal Materials

We shall consider two cases of tetragonal structures, one for which $c/a > 1$ and the second for which $c/a < 1$. The lattice parameters will be restricted so as the atomic volume is constant and the tight-binding parameters, both hopping and hybridization, are assumed to decrease inversely with the interatomic spacings as the spacings are increased. It turns out, when $c > a$, the direct hopping processes induce a quasi-two-dimensional character to the conduction and the $5f$ bands. However, the hybridization between the conduction and $5f$ bands has the effect of an inter-planar coupling. Because of the dependence of the hybridization Slater-Koster parameter on the direction cosines and the dependence of the dispersion relation on the modulus squared of the hybridization matrix elements, the z-band hybridizes preferentially with the conduction band. For $c < a$, the direct hopping process induce one-dimensional characters in the dispersion relations and the hybridization couples the states of the quasi-one-dimensional chains, however, the x and y band are preferentially mixed with the conduction band states.

For $c/a > 1$, the dimensionless partial densities of states $\rho^{\alpha}(\omega)t$ versus ω/t are shown in Fig. 3.7 for $V = 0.15t$, $U = 0.9t$ and for $V = 0.6t$, $U = 1.3t$ respectively. It is seen that the three-fold degeneracy of the sub-bands is lifted. The tail of the z sub-band extends to the lowest edge of the conduction band, whereas the tail of the two-fold degenerate x and y sub-bands drops precipitously at an energy where the conduction band exhibits a van Hove singularity. The centroid of the z sub-band is shifted to a higher energy than the x and y sub-bands. This indicates the z sub-band experiences a stronger mixing and level repulsion due to the hybridization. The spin-orbit splitting is more evident for smaller values of the hybridization and, as is seen in Fig. 3.8 , the ratio of the projected j weights shows a resonant-like structure in

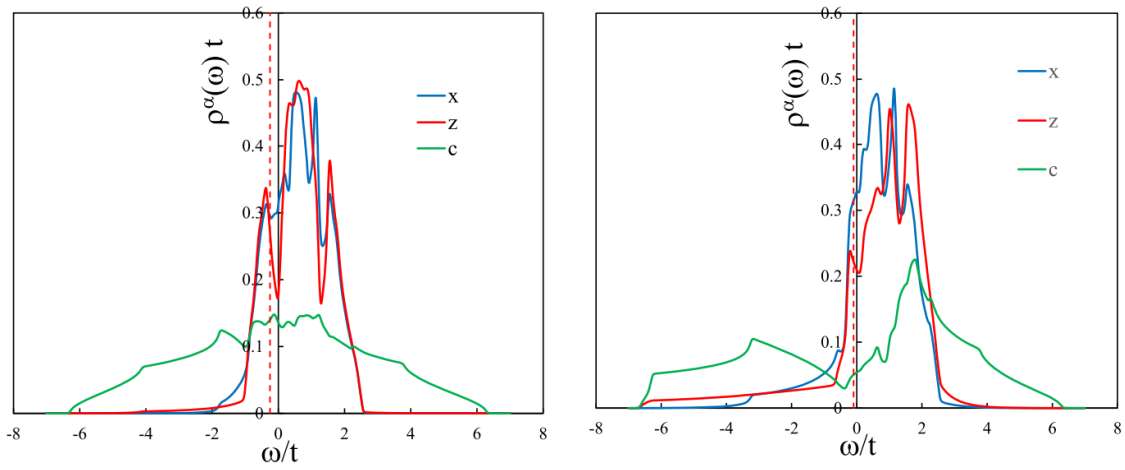

Figure 3.7: The dimensionless partial densities of states $\rho^{\alpha}(\omega)t$ in the tetragonal basis for $c = 2a$ calculated for $V = 0.15t$, $U = 0.9t$ (left) and for $V = 0.6t$, $U = 1.3t$ (right).

an energy interval around the gaps which is less distinct than in the cubic case which means the reduced degeneracy. Fig. 3.9 shows the magnitudes of the off-diagonal

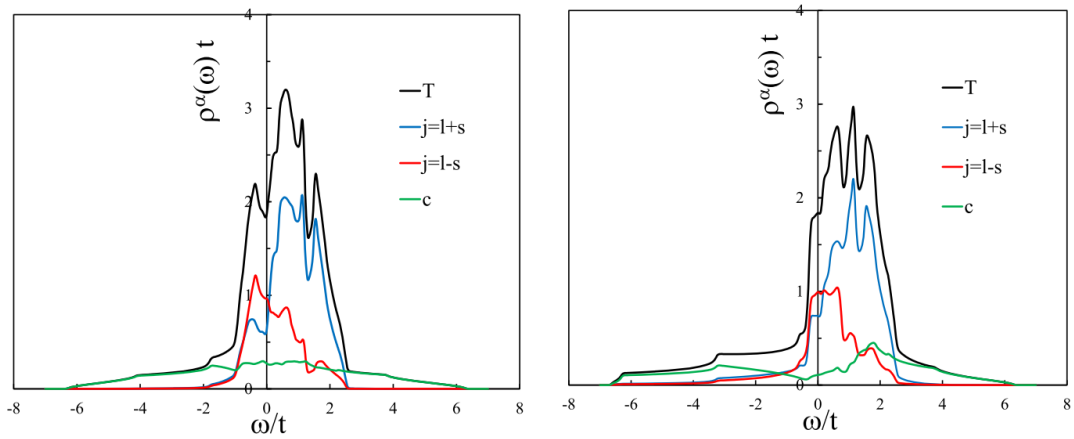

Figure 3.8: The dimensionless total density of states $\rho^{T}(\omega)t$ and its decomposition into partial densities of states $\rho_{\alpha}(\omega)t$ for $V = 0.15t$, $U = 0.9t$ (left) and for $V = 0.6t$, $U = 1.3t$ (right) with $j = l \pm s$ for $c = 2a$.

correlations as a function of μ/t. The magnitudes of the spin-flip correlations $\langle f^{\dagger}_{x,\downarrow} f_{y,\uparrow} \rangle$ and $\langle f^{\dagger}_{z,\uparrow} f_{y,\downarrow} \rangle$ are identical. The magnitude of the non-spin-flip correlation $\langle f^{\dagger}_{y,\uparrow} f_{x,\uparrow} \rangle$ shows a higher and narrower peak than the spin-flip correlations, indicating that there is a higher degree of generacy of the dispersion relations of the x and y sub-bands.

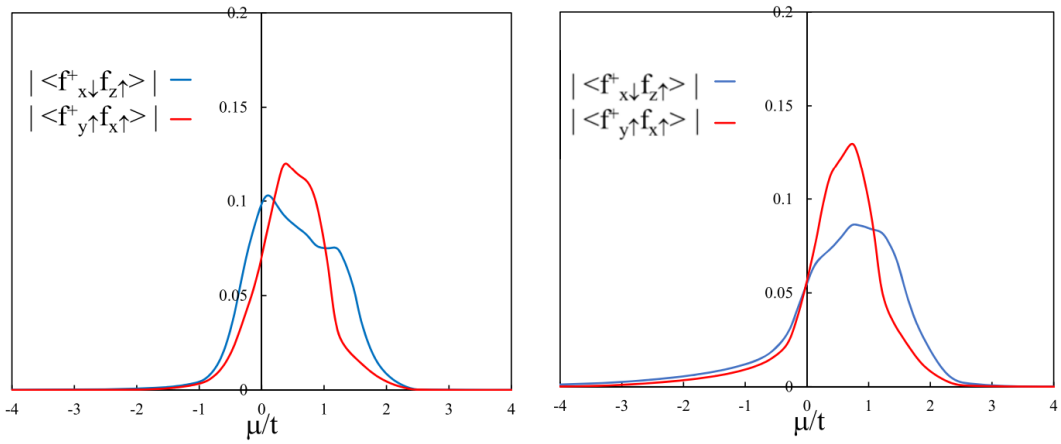

Figure 3.9: The magnitudes of the off-diagonal spin–orbit correlations calculated for $c = 2a$ for $V = 0.15t$, $U = 0.9t$ (left) and $V = 0.75t$, $U = 1.93t$ (right).

For $V = 0.15t$, the x and y components of the spin-orbit interaction are enhanced by a factor of 1.5 while the z-component is enhanced by a factor of 1.3. The anisotropy of the interaction is reduced for larger values of V. The smaller value of λ_z compared with λ_x has the effect of increasing the anisotropy of the magnetic susceptibility.

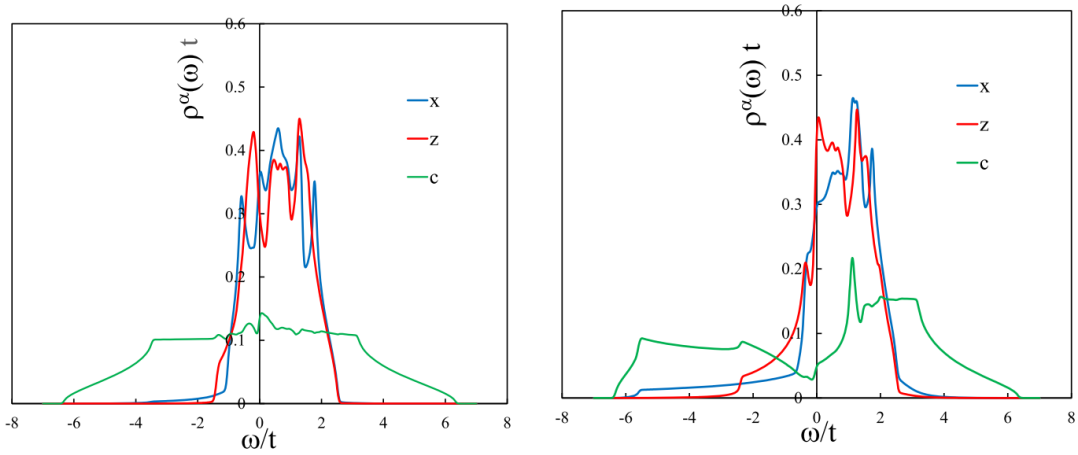

Figure 3.10: The dimensionless partial densities of states $\rho^{\alpha}(\omega)t$ for $V = 0.15t$, $U = 1.1t$ (left) and $V = 0.6t$, $U = 1.35t$ for the case where $c = a/2$.

For $c < a$, in Fig. 3.10 the densities of states show more structure associated with the one-dimensional characters of the conduction and $5f$ bands which produce peaks

at the edges of the bands. In contrast to the case where $c > a$, it is seen that the x and y sub-bands are more strongly hybridized than the z sub-band. Due to the structure

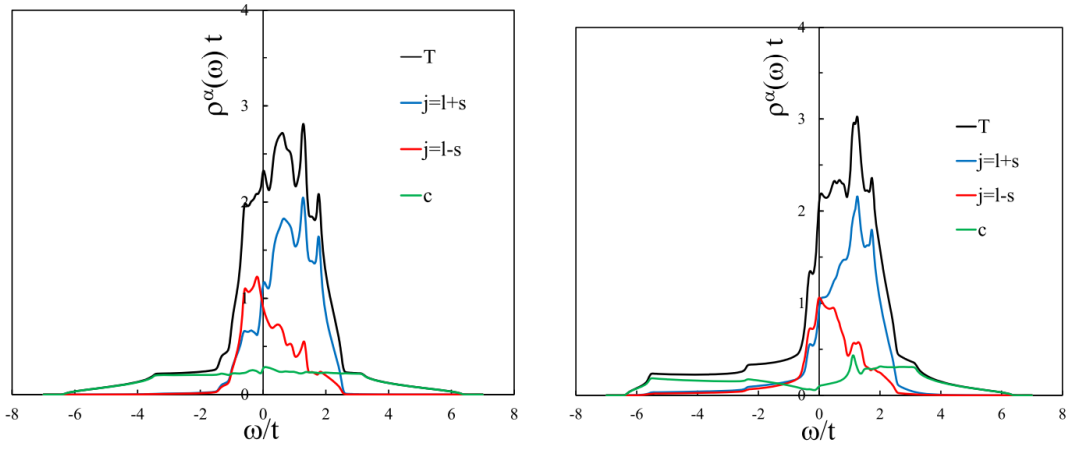

Figure 3.11: The dimensionless total density of states $\rho^T(\omega)t$ and its decomposition into partial densities of states $\rho^\alpha(\omega)t$ with $j = l \pm s$ and $c = a/2$ for $V = 0.15t$, $U = 1.1t$ (left) and $V = 0.6t$, $U = 1.35t$ (right).

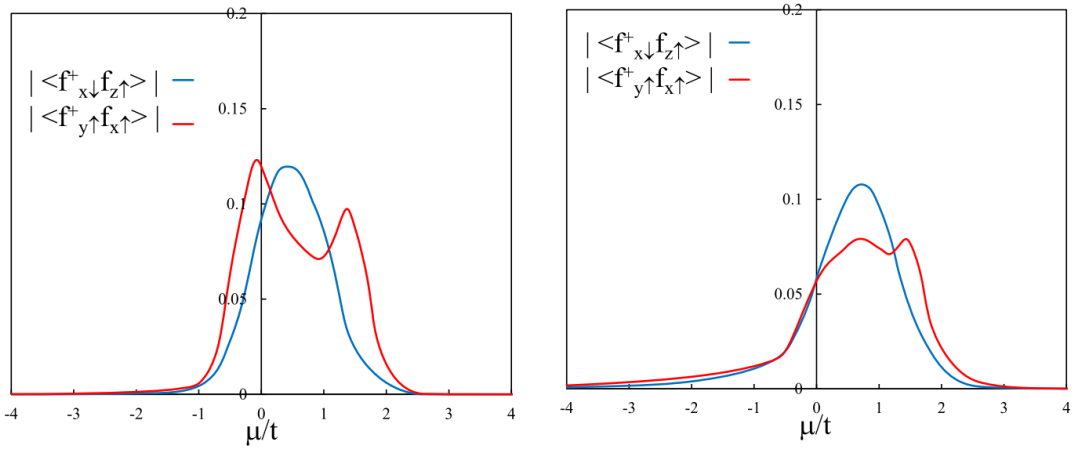

Figure 3.12: The magnitudes of the off-diagonal spin–orbit correlations calculated for $c = a/2$ for $V = 0.15t$, $U = 1.1t$ (left) and $V = 0.6t$, $U = 1.35t$ (right).

in the density of states, the spin-orbit resonances are only identifiable through the resonance by the projection onto the j states in Fig. 3.11. The magnitudes of the off-diagonal spin-orbit correlations shown in Fig. 3.12 indicate that the enhancement

of the z component of the spin-orbit coupling are larger than the x, y correlation shows a double peaked structure, which is most pronounced for small hybridization strengths.

3.5 Discussion

While the origin of the spin-orbit coupling is firmly entrenched in the relativistic theory of atomic structure, its manifestation in solids is quite different and is intimately tied to the electronic dispersion relations. This is illustrated by considering the extreme case of tetragonal anisotropy of the above model. For $c/a \gg 1$, the z-orbitals form two-dimensional bands which are weakly hybridized to the two-dimensional conduction band. In this extreme limit, the coupling of the x and y orbitals with the conduction band can be neglected, because of the dependence of the hybridization matrix elements on the direction cosines. The orbital selective nature of the hybridization is a distinguishing feature of the underscreened Anderson model [31, 32, 33]. Due to the characteristic shapes of the orbitals, the Slater-Koster parameters for the x sub-band have e different dispersions along the k_x and k_y directions and, due to C_4 symmetry, the dispersion of the y sub-band is simply related to the dispersion of the x sub-band by a rotation of $\frac{\pi}{2}$. Therefore, the dispersion relations become degenerate on the lines $k_x = \pm k_y$. In this situation, the λ_z-component of the spin-orbit coupling lifts the four-fold degeneracy along the lines, producing two two-fold degenerate spin-orbit split bands which, when combined with the van Hove singularities, produce the features in the density of states. This illustration shows that spin-orbit resonances are most evident in materials where the bands exhibit nesting at energies either above or below the Fermi energy.

Since both the Coulomb interaction U and the spin-orbit interaction produce

spin-flip inter-orbital scattering of electrons in hybridized Bloch bands, these two scattering amplitudes act coherently to produce an enhanced spin-orbit coupling. The correlations induced by the Coulomb interaction are increased cooperatively, in a way similar to that in which U, together with J, induces magnetism. For an anisotropic system, the spin-orbit resonances induce sizeable ground-state correlations which are amplified by the Coulomb interaction. The induced correlations selectively enhance the components of the spin-orbit interaction and the magnetic materials. Furthermore, since antiferromagnetism is frequently related to the nesting of bands at the Fermi energy, materials that are close to antiferromagnetic quantum critical points are also candidate materials for observing spin-orbit gaps near Fermi energy.

3.6 Summary

We have demonstrated that Coulomb correlations enhance the spin-orbit interaction in strongly correlated $5f$ metals and have shown that the enhancements are greatest for materials close to magnetic quantum critical points. Because of the importance of the nonlinear nature of the enhancement, giant enhancements are only expected for materials containing elements from the first half of the actinide series. Furthermore, the enhancements are anisotropic in non-cubic materials. For tetragonal crystals with $c > a$, we have found that the strengths of the components of the spin-orbit coupling satisfy the inequalities $\lambda_x = \lambda_y > \lambda_z$, while for $a > c$, $\lambda_z > \lambda_x = \lambda_y$. In addition, we have shown that the density of states should show features indicative of the enhanced spin-orbit gaps in the one-electron density of states, which should be observable in electron spectroscopies. However, off Fermi-surface gaps are expected to be severely broadened by the effects of inelastic scattering processes. Nevertheless, BIS experiments on uranium and plutonium based materials have found off Fermi-

energy peak-dip structures which are interpretable in terms of enhanced spin-orbit coupling.

CHAPTER 4

NONLINEAR RASHBA EFFECT IN A STRONGLY CORRELATED SYSTEM

There have been several reports of experimental observations of a field-dependent enhancement of the Rashba spin-orbit splitting in surface states. We show that strong Coulomb correlation leads to an enhancement of the spin-orbit coupling which is highly sensitive to band-bending and applied electric potentials. In a system with broken inversion symmetry, this leads to a nonlinear field-dependent Rashba interaction that could be responsible for the experimental observations. The main part of this chapter has been submitted to a journal for review.

4.1 Introduction

The Rashba spin-orbit coupling occurs in systems which have broken inversion symmetry and can lift the degeneracy of surface states. It plays an important role in spintronics applications [50]. It is generally treated using a non-interacting description [51, 52] which always produces a linear electric-field-dependent Rashba effect [3, 53]. It has been suggested that strong Coulomb interactions will produce an increase in the effective mass that decrease the strength of the Rashba spin-orbit coupling in sys-

tems with broken inversion symmetry [54] while, by contrast, it has been suggested that the Coulomb interactions may lead to a modestly enhanced spin-orbit coupling in a low-density two-dimensional free electron gas [55]. By contrast, an enhancement by factor of the order of $4 \sim 10$ are needed to explain the giant enhancements found in various experiments [54, 56, 57, 58, 59, 60].

Here we shall show that the effects of strong Coulomb correlations can enhance the spin-orbit coupling and, in inversion symmetry broken systems, may lead to a giant Rashba effect. The basic reason why Coulomb interactions enhance the spin-orbit interactions, is that the interactions act coherently in the scattering of Bloch electrons. This can be most easily visualized in a mean-field treatment [14] which retains off-diagonal correlations in the Coulomb interaction. These off-diagonal correlations have the same symmetry as the spin-orbit interaction, so the scattering of the electron wave functions by the off-diagonal Coulomb interactions and the spin-orbit coupling is constructive. This scattering becomes resonant at the energies where the Bloch states are nearly degenerate [40], and can lead to a large enhancement of the spin-orbit coupling. Furthermore, we show that the enhancement is highly field-dependent, which can produce a giant and nonlinear field-dependent Rashba coupling.

Firstly we shall model the electronic states by a tight-binding model of the electronic states of triangular lattice which are subject to atomic spin-orbit coupling, short-ranged Coulomb interactions and an inversion-symmetry-breaking term. This will be followed by a mean-field treatment of the Hamiltonian, in which the interaction is allowed to adapt to the symmetry of the electronic system. This is in direct contrast to the non-spin-polarized density functional theory [57] in which the exchange-correlation function does not incorporate the spin-orbital symmetry and underestimates the magnitude of the observed giant enhancements by one or two orders of magnitude [61, 62, 63, 64, 65]. We shall show how the enhanced spin-orbit

interaction leads to the Rashba coupling. Finally, we shall present and discuss the numerical results, and show how to use Feynman diagrams to understand how the spin-orbit interaction can be enhanced by the on-site Coulomb interaction.

4.2 Model Hamiltonian

The model Hamiltonian is written as

$$\hat{H} = \hat{H}_0 + \hat{H}_{SO} + \hat{H}_{int} + \hat{H}_E, \tag{4.1}$$

where the first term describes the dispersion relationship of the non-interacting electrons. Here, we consider a typical two-dimensional triangular lattice, such as the Au (111) surface [66, 64], setting primitive vectors as $\boldsymbol{a_1} = (1, 0)$ and $\boldsymbol{a_2} = (1/2, \sqrt{3}/2)$. We only consider the nearest-neighbor hopping between p orbitals, which is represented by $\hat{H}_0$, which can be written as

$$\hat{H}_0 = \sum_{\langle i,j\rangle,\alpha,\beta,\sigma} t_{\alpha\beta,ij} a^{\dagger}_{i\alpha,\sigma} a_{j\beta,\sigma} + h.c., \tag{4.2}$$

where the hopping matrix elements are given by

$$\begin{aligned}
t_{xx,ij} &= l^2 V_{pp\sigma} + m^2 V_{pp\pi}, \\
t_{yy,ij} &= m^2 V_{pp\sigma} + l^2 V_{pp\pi}, \\
t_{zz,ij} &= V_{pp\pi}, \\
t_{xy,ij} &= lm(V_{pp\sigma} - V_{pp\pi}),
\end{aligned}$$

where l and m are the directional cosines of the vector connecting neighboring atoms. We shall denote $t_\sigma = V_{pp\sigma}$, $t_\pi = -V_{pp\pi}$. The hopping terms, $\hat{H}_0$, has the explicit

momentum space form

$$\begin{aligned}\hat{H}_0 =& \sum_{\boldsymbol{k},\sigma} \epsilon_{\boldsymbol{k},x}\ a^\dagger_{\boldsymbol{k},x,\sigma} a_{\boldsymbol{k},x,\sigma} + \sum_{\boldsymbol{k},\sigma} \epsilon_{\boldsymbol{k},y} a^\dagger_{\boldsymbol{k},y,\sigma} a_{\boldsymbol{k},y,\sigma} + \sum_{\boldsymbol{k},\sigma} \epsilon_{\boldsymbol{k},z} a^\dagger_{\boldsymbol{k},z,\sigma} a_{\boldsymbol{k},z,\sigma} \\ &+ \sum_{\boldsymbol{k},\sigma} t_{x,y,\boldsymbol{k}} \left(a^\dagger_{\boldsymbol{k},x,\sigma} a_{\boldsymbol{k},y,\sigma} + a^\dagger_{\boldsymbol{k},y,\sigma} a_{\boldsymbol{k},x,\sigma} \right).\end{aligned} \tag{4.3}$$

where the sub-band dispersion relations are given by

$$\epsilon_{\boldsymbol{k},x} = 2t_\sigma \cos k_x + (t_\sigma - 3t_\pi) \cos\frac{k_x}{2} \cos\frac{\sqrt{3}k_y}{2}, \tag{4.4}$$

$$\epsilon_{\boldsymbol{k},y} = -2t_\pi \cos k_x + (3t_\sigma - t_\pi) \cos\frac{k_x}{2} \cos\frac{\sqrt{3}k_y}{2}, \tag{4.5}$$

$$\epsilon_{\boldsymbol{k},z} = -2t_\pi \cos k_x - 4t_\pi \cos\frac{k_x}{2} \cos\frac{\sqrt{3}k_y}{2}, \tag{4.6}$$

and the mixing term is expressed as

$$t_{x,y,\boldsymbol{k}} = -\sqrt{3}(t_\sigma + t_\pi) \sin\frac{k_x}{2} \sin\frac{\sqrt{3}k_y}{2}. \tag{4.7}$$

The term $\hat{H}_{SO}$ describes the intra-atomic spin-orbit interactions,

$$\begin{aligned}\hat{H}_{SO} =& \frac{\lambda_z}{2} \sum_{\boldsymbol{k},\sigma} i\sigma \left(a^\dagger_{\boldsymbol{k},y,\sigma} a_{\boldsymbol{k},x,\sigma} - a^\dagger_{\boldsymbol{k},x,\sigma} a_{\boldsymbol{k},y,\sigma} \right) - \frac{\lambda_y}{2} \sum_{\boldsymbol{k},\sigma} \sigma \left(a^\dagger_{\boldsymbol{k},z,\sigma} a_{\boldsymbol{k},x,\overline{\sigma}} + a^\dagger_{\boldsymbol{k},x,\overline{\sigma}} a_{\boldsymbol{k},z,\sigma} \right) \\ &+ \frac{\lambda_x}{2} \sum_{\boldsymbol{k},\sigma} i \left(a^\dagger_{\boldsymbol{k},z,\sigma} a_{\boldsymbol{k},y,\overline{\sigma}} - a^\dagger_{\boldsymbol{k},y,\overline{\sigma}} a_{\boldsymbol{k},z,\sigma} \right),\end{aligned} \tag{4.8}$$

where, in the atomic limit, $\lambda_\alpha = \lambda_0$. The spin-orbit interaction λ_α will become anisotropic when enhanced by the Coulomb interactions.

The third term is the on-site Coulomb interaction

$$\hat{H}_{int} = \frac{1}{2} \sum_{i,\alpha \neq \beta,\sigma} U \hat{n}_{i,\alpha,\sigma} \hat{n}_{i,\beta,\sigma} + \frac{1}{2} \sum_{i,\alpha,\beta,\sigma} U \hat{n}_{i,\alpha,\sigma} \hat{n}_{i,\beta,\overline{\sigma}}. \tag{4.9}$$

The final term $\hat{H}_E$ breaks the inversion symmetry. It can be simply understood as the effect of a potential gradient on the surface or the interface induced by surface charges. The induced electric field breaks the inversion symmetry of the p orbitals, thereby allowing the p_z electrons to hop onto the p_x and p_y orbitals. The field induced hopping matrix elements can be expressed as

$$t_{xz,ij} = l\delta,$$
$$t_{yz,ij} = m\delta.$$

Therefore, the symmetry breaking term, $\hat{H}_E$, can be written as

$$\begin{aligned} \hat{H}_E =& 2i\delta \sum_{\boldsymbol{k},\boldsymbol{\sigma}} \left(\sin k_x + \sin \frac{k_x}{2} \cos \frac{\sqrt{3} k_y}{2} \right) \left(a^{\dagger}_{\boldsymbol{k},z,\sigma} a_{\boldsymbol{k},x,\sigma} - a^{\dagger}_{\boldsymbol{k},x,\sigma} a_{\boldsymbol{k},z,\sigma} \right) \\ &+ 2\sqrt{3} i\delta \sum_{\boldsymbol{k}} \cos \frac{k_x}{2} \sin \frac{\sqrt{3} k_y}{2} \left(a^{\dagger}_{\boldsymbol{k},z,\sigma} a_{\boldsymbol{k},y,\sigma} - a^{\dagger}_{\boldsymbol{k},y,\sigma} a_{\boldsymbol{k},z,\sigma} \right). \end{aligned} \tag{4.10}$$

The dispersion relation for the electronic bands is shown in Fig. 4.1 . The partial density of states shown in Fig. 4.2 exhibits a van Hove singularity in the density of states. For the case of almost filled bands, the Fermi surface is highly nested as is seen in Fig. 4.3 . Therefore, one expects that the surface may reconstruct leading to a structure with long-ranged doping-dependent periodicity.

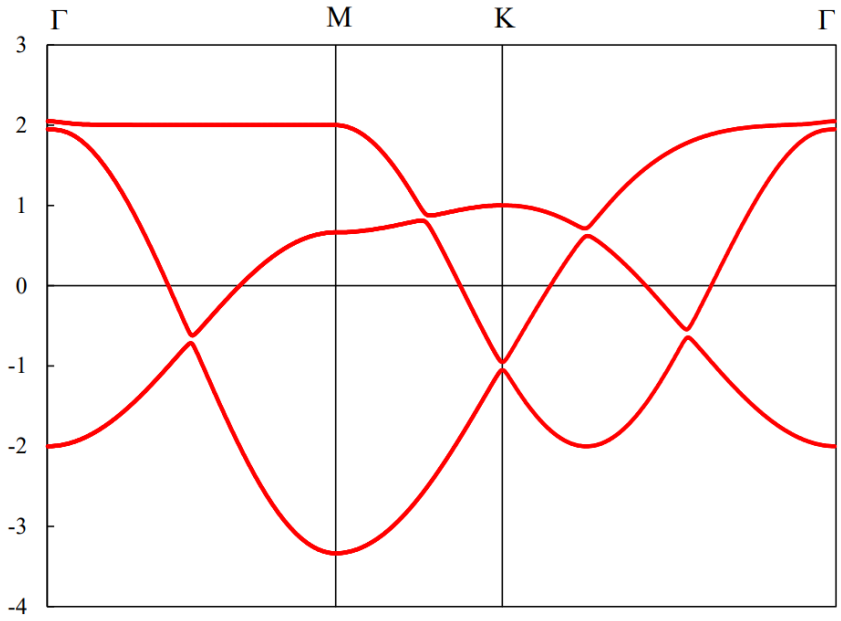

Figure 4.1: The calculated electronic dispersion relations. The p_z orbital has the narrowest band-width and contributes the lowest branch at the Γ point.

4.3 Mean-field Approximation

Using the mean-field approximation, the on-site Coulomb interaction renormalizes the non-interacting Hamiltonian by the terms

$$\hat{H}_{MF} = \sum_{\alpha,\beta,\sigma,\sigma'} \Phi^{\alpha,\beta}_{\sigma,\sigma'} a^{\dagger}_{\alpha,\sigma} a_{\beta,\sigma'}. \tag{4.11}$$

In the absence of spontaneous symmetry breaking, the diagonal parts of the mean-field Hamiltonian are modified by the interaction by additive terms that are proportional to the occupation number. The diagonal terms do not play a significant role in the physics discussed here. The off-diagonal parts have the same form as the spin-orbit

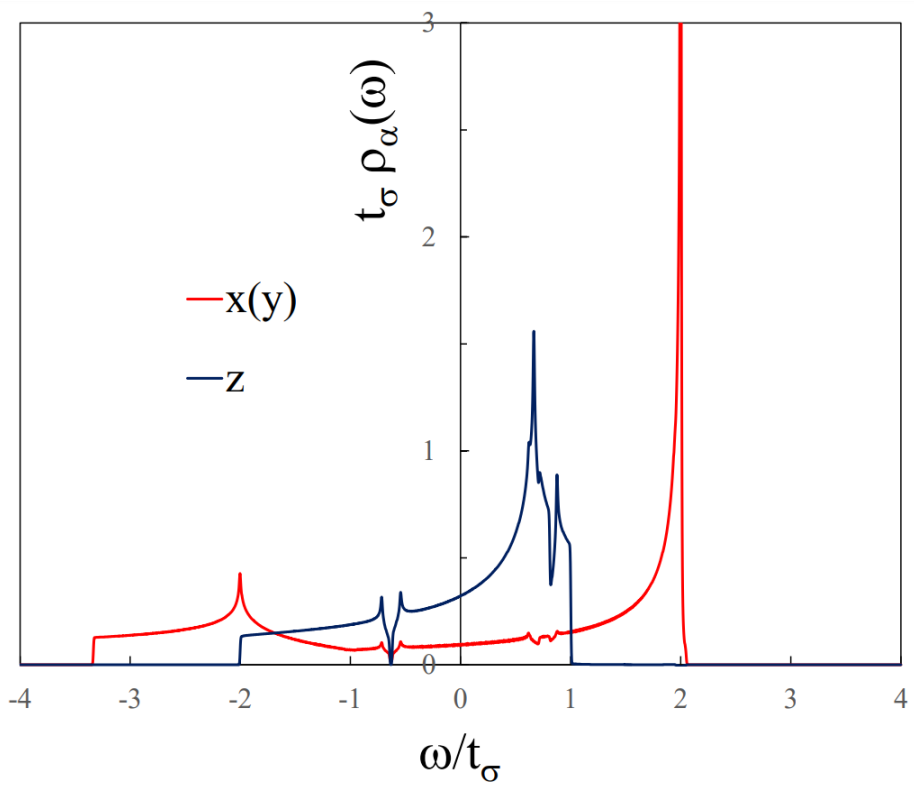

Figure 4.2: The dimensionless partial density of states, $\rho_\alpha(\omega)$, per orbital per spin.

interaction, and are given by

$$\Phi^{x,y}_{\sigma,\sigma} = -\,U\,\langle a^\dagger_{i,y,\sigma} a_{i,x,\sigma}\rangle\,, \tag{4.12}$$

$$\Phi^{z,x}_{\bar{\sigma},\sigma} = -\,U\,\langle a^\dagger_{i,z,\bar{\sigma}} a_{i,x,\sigma}\rangle\,, \tag{4.13}$$

$$\Phi^{y,z}_{\bar{\sigma},\sigma} = -\,U\,\langle a^\dagger_{i,z,\sigma} a_{i,y,\bar{\sigma}}\rangle\,. \tag{4.14}$$

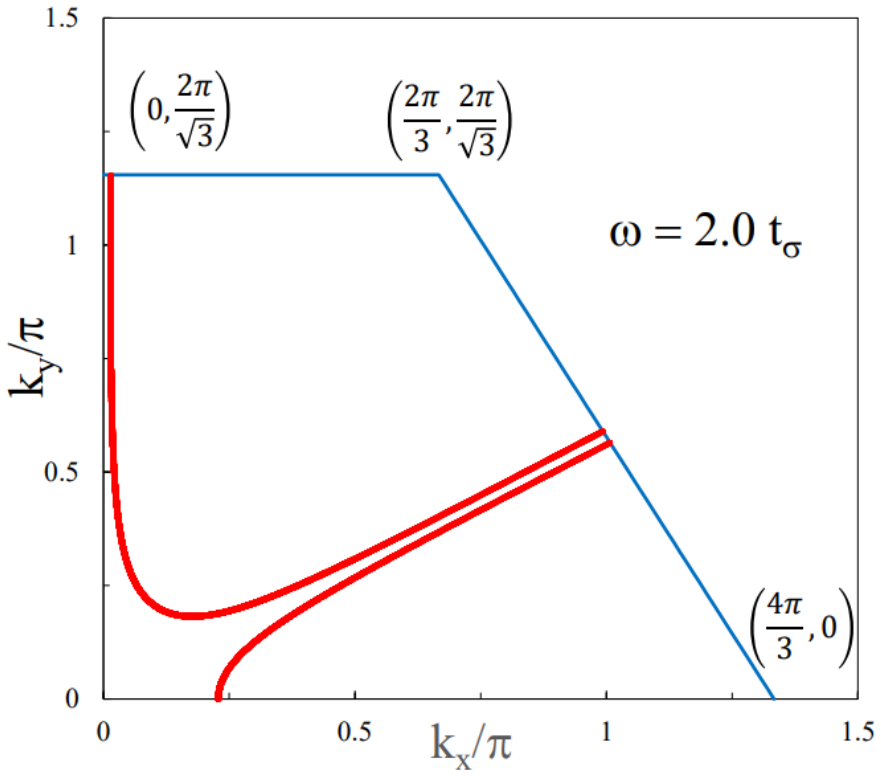

Figure 4.3: A constant energy section of the Brillouin zone which corresponds to the van Hove singularity at $\omega = 2.0t_\sigma$.

The off-diagonal correlations are calculated from the Green's functions that are expressible as

$$G_{x,\sigma,y,\sigma}(\boldsymbol{k},\omega) = \left((-i\frac{\sigma\lambda_z}{2} + t_{x,y,\boldsymbol{k}})(\omega - \epsilon_{z,\boldsymbol{k}}) + i\frac{\sigma\lambda_x\lambda_y}{4}\right)/D_3(\boldsymbol{k},\omega), \tag{4.15}$$

$$G_{x,\sigma,z,\bar{\sigma}}(\boldsymbol{k},\omega) = \left(\frac{\sigma\lambda_y}{2}(\omega - \epsilon_{y,\boldsymbol{k}}) - \frac{\sigma\lambda_x\lambda_z}{4} - i\frac{\lambda_x}{2}t_{x,y,\boldsymbol{k}}\right)/D_3(\boldsymbol{k},\omega), \tag{4.16}$$

$$G_{y,\sigma,z,\bar{\sigma}}(\boldsymbol{k},\omega) = \left(-i\frac{\lambda_x}{2}(\omega - \epsilon_{x,\boldsymbol{k}}) + i\frac{\lambda_y\lambda_z}{4} + \frac{\sigma\lambda_y}{2}t_{x,y,\boldsymbol{k}}\right)/D_3(\boldsymbol{k},\omega). \tag{4.17}$$

where the denominator $D_3(\boldsymbol{k},\omega)$ is given by

$$\begin{aligned} D_3(\boldsymbol{k},\omega) =& \omega^3 - \omega^2(\epsilon_{x,\boldsymbol{k}} + \epsilon_{y,\boldsymbol{k}} + \epsilon_{z,\boldsymbol{k}}) \\ &+ \omega\left(\epsilon_{x,\boldsymbol{k}}\epsilon_{y,\boldsymbol{k}} + \epsilon_{y,\boldsymbol{k}}\epsilon_{z,\boldsymbol{k}} + \epsilon_{z,\boldsymbol{k}}\epsilon_{x,\boldsymbol{k}} - t^2_{x,y,\boldsymbol{k}} - \frac{1}{4}(\lambda_x^2 + \lambda_y^2 + \lambda_z^2)\right) \\ &- \epsilon_{x,\boldsymbol{k}}\epsilon_{y,\boldsymbol{k}}\epsilon_{z,\boldsymbol{k}} + \frac{1}{4}(\epsilon_{x,\boldsymbol{k}}\lambda_x^2 + \epsilon_{y,\boldsymbol{k}}\lambda_y^2 + \epsilon_{z,\boldsymbol{k}}\lambda_z^2) + \frac{\lambda_x\lambda_y\lambda_z}{4} + \epsilon_{z,\boldsymbol{k}}t^2_{x,y,\boldsymbol{k}} \end{aligned} \tag{4.18}$$

The zeroes of $D_3(\boldsymbol{k},\omega)$ yield the electronic dispersion relations. The off-diagonal correlations have the form of a generalized susceptibility in which the numerators have the same symmetries as the spin-orbit coupling, since the terms proportional to $t_{x,y}$ vanish due to inversion symmetry. Therefore, the enhanced spin-orbital coupling strengths are given by

$$\lambda_z = \lambda_0 - 2i\sigma\Phi^{x,y}_{\sigma,\sigma}, \tag{4.19}$$

$$\lambda_y = \lambda_0 + 2\sigma\Phi^{z,x}_{\bar{\sigma},\sigma}, \tag{4.20}$$

$$\lambda_x = \lambda_0 + 2i\sigma\Phi^{y,z}_{\bar{\sigma},\sigma}. \tag{4.21}$$

Thus, the spin-orbit interaction induces Coulomb correlations to participate coherently in the scattering of Bloch electrons and results in an enhancement of the spin-orbit coupling strength.

The effective Rashba Hamiltonian near the Γ point can be obtained by second-order perturbation expansion. Spin-flip scattering from the $p_{z,\downarrow}$ orbital to the $p_{z,\uparrow}$

orbital can be evaluated by below processes

$$\frac{\langle z,\uparrow|3i\delta k_x a^\dagger_{\boldsymbol{k},z,\uparrow}a_{\boldsymbol{k},x,\uparrow}|x,\uparrow\rangle\langle x,\uparrow|\lambda_y/2a^\dagger_{\boldsymbol{k},x,\uparrow}a_{\boldsymbol{k},z,\downarrow}|z,\downarrow\rangle}{\epsilon_{z,\boldsymbol{k}}-\epsilon_{x,\boldsymbol{k}}}, \tag{4.22}$$

$$\frac{\langle z,\uparrow|-\lambda_y/2a^\dagger_{\boldsymbol{k},z,\uparrow}a_{\boldsymbol{k},x,\downarrow}|x,\downarrow\rangle\langle x,\downarrow|-3i\delta k_x a^\dagger_{\boldsymbol{k},x,\downarrow}a_{\boldsymbol{k},z,\downarrow}|z,\downarrow\rangle}{\epsilon_{z,\boldsymbol{k}}-\epsilon_{x,\boldsymbol{k}}}, \tag{4.23}$$

$$\frac{\langle z,\uparrow|3i\delta k_y a^\dagger_{\boldsymbol{k},z,\uparrow}a_{\boldsymbol{k},y,\uparrow}|y,\uparrow\rangle\langle y,\uparrow|-i\lambda_x/2a^\dagger_{\boldsymbol{k},y,\uparrow}a_{\boldsymbol{k},z,\downarrow}|z,\downarrow\rangle}{\epsilon_{z,\boldsymbol{k}}-\epsilon_{y,\boldsymbol{k}}}, \tag{4.24}$$

$$\frac{\langle z,\uparrow|i\lambda_x/2a^\dagger_{\boldsymbol{k},z,\uparrow}a_{\boldsymbol{k},y,\downarrow}|y,\downarrow\rangle\langle y,\downarrow|-3i\delta k_y a^\dagger_{\boldsymbol{k},y,\downarrow}a_{\boldsymbol{k},z,\downarrow}|z,\downarrow\rangle}{\epsilon_{z,\boldsymbol{k}}-\epsilon_{y,\boldsymbol{k}}}. \tag{4.25}$$

Sum all the terms, and the total scattering strength is

$$\frac{-i\lambda_y\delta k_x-\lambda_x\delta k_y}{t_\pi+t_\sigma}. \tag{4.26}$$

Correspondingly, strength of scattering from the $p_{z,\uparrow}$ orbital to the $p_{z,\downarrow}$ orbital is

$$\frac{i\lambda_y\delta k_x-\lambda_x\delta k_y}{t_\pi+t_\sigma}. \tag{4.27}$$

The effective Hamiltonian is

$$\mathcal{H}_R=\frac{\lambda_{x(y)}\delta}{t_\pi+t_\sigma}(k_x\sigma_y-k_y\sigma_x)+\mathcal{O}(\boldsymbol{k}^2). \tag{4.28}$$

The Rashba constant is expressed as $\alpha_R=\frac{\lambda_{x(y)}\delta}{t_\pi+t_\sigma}$. In the absence of Coulomb interaction, α_R changes linearly with electric field as expected since it only effects δ. However, in a strongly correlated system, the application of electric field or equivalently tuning chemical potential changes the occupation numbers of the orbitals. In this situation, we have an enhanced spin-orbital coupling strength, which would lead to possible nonlinear Rashba effects.

4.4 Results and Discussion

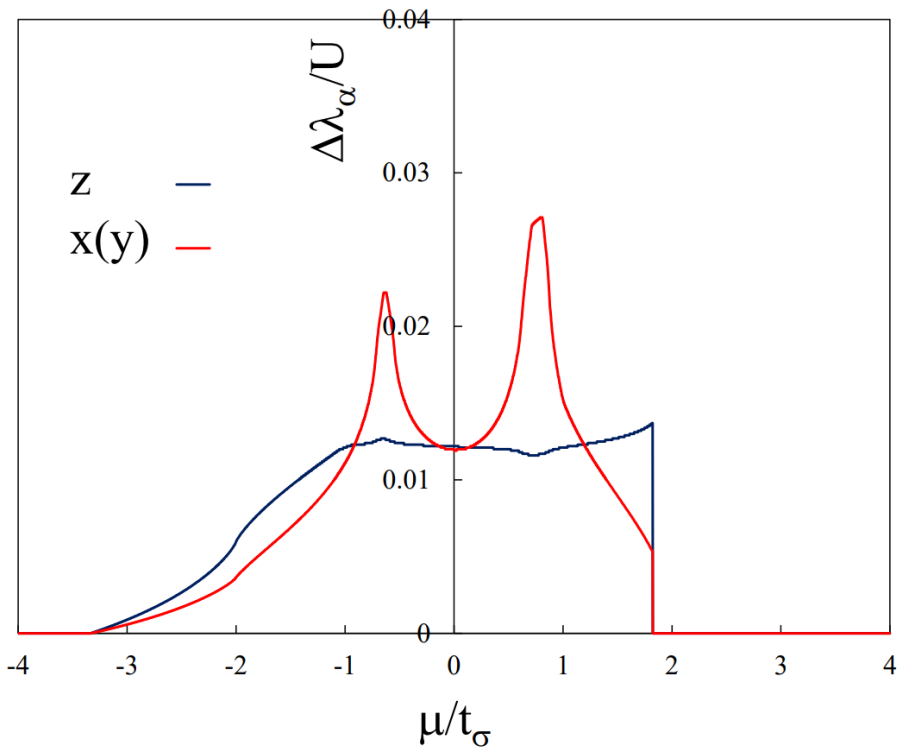

Figure 4.4: The dimensionless increase of the components of the spin-orbit interaction, $\Delta\lambda_\alpha$.

The numerical results were obtained for the parameter values of $t_\sigma = 1, t_\pi = 1/3$, and $\lambda_0 = 0.1$. Fig. 4.1 depicts the electronic dispersion relations. In the absence of the perturbing terms, the p_z band is decoupled from the p_x and p_y bands. The p_z band has the smallest bandwidth. The p_x and p_y bands are almost degenerate at the Γ point, but, due to the orientation dependence of the tight-binding parameters, the degeneracy is lifted at generic k-points. The hexagonal symmetry of the Brillouin zone leads to the equality of the p_x and p_y partial densities of states, as seen in Fig. 4.2. It should be noted that the spin-orbit interaction lifts the band degeneracy at the band crossings, and this is accompanied by the appearance of the pseudogaps that are seen

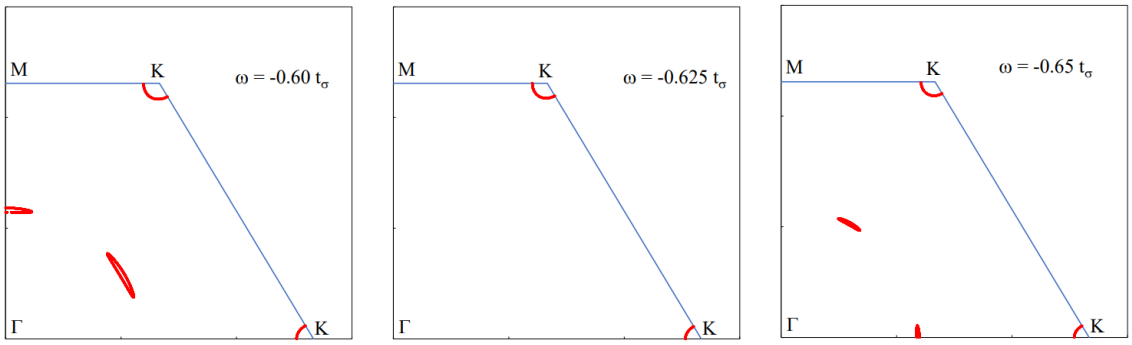

Figure 4.5: Constant energy sections of the Brillouin zone energies near $\omega = -0.625t_\sigma$, indicating the existence of two Lifshitz transitions.

in the electronic density of states. These pseudogaps occur at energies at which the integrated density of states corresponds to an occupation of approximately two and four electrons per atom. The enhanced spin-orbit coupling is shown in Fig. 4.4 as a function of the chemical potential μ. It is seen that the enhancement is resonant when the Fermi-energy is associated with the pseudogaps in the density of states caused by Lifshitz transitions. However, the enhancement is largest for the pseudogap with the largest residual density of states, which is a signature of the enhancement being caused by the coherent scattering of the itinerant electrons.

Since the expectation values of the off-diagonal correlation are functions of chemical potential, it is possible to change them by applying an electric field or by chemical doping. In Fig. 4.4, it is clear that in most regions the spin-flip components of the spin-orbit coupling λ_x is approximately linearly proportional to the chemical potential, but when near $\mu = -0.6t_\sigma$, the relation becomes highly nonlinear and then starts to drop at the higher values of μ where it saturates. The constant energy sections near this point have been plotted in Fig. 4.5. Since the Rashba coupling primarily involves the spin-flip component of the spin-orbit coupling that undergoes a resonant enhancement, the Rashba spin-orbit coupling should also exhibit a giant and non-linear dependence on the applied electric field. When *s*-*p* metals are expected to

neither have strong spin-orbit interactions nor strong Coulomb interactions, the materials in which the field-dependent Rashba effect have been observed involve d states near the Fermi energy [54, 57, 60, 66]. Since the $3d$ orbitals are highly localized, it is conceivable that there is a non-negligible admixture of $3d$ states below the Fermi energy and that the induced correlations are responsible for the observed effects.

4.5 Feynman Diagrams

The enhancement of spin-orbit coupling by on-site Coulomb interaction can be understood by Feynman diagrams instead of by the pure algebraic way.

4.5.1 Imaginary-time Green's Functions

Replace real time by imaginary time

$$it \to \tau. \tag{4.29}$$

Single-particle Green's function is defined as

$$G_{ab}(\tau - \tau') = -\langle \hat{T}\psi_a(\tau)\psi_b^\dagger(\tau')\rangle\,, \tag{4.30}$$

where ψ represents either a fermionic or a bosonic field. For non-interacting particles, the Hamiltonian can be diagonal, which can be expressed in momentum space as

$$\hat{H}_0 = \sum_{\mathbf{k}} \epsilon_{\mathbf{k}} c_{\mathbf{k}}^\dagger c_{\mathbf{k}}. \tag{4.31}$$

In the Heisenberg picture, the creation and annihilation operators are time-dependent

$$c_{\mathbf{k}}^{\dagger}(\tau) = e^{\tau \hat{H}_0} c_{\mathbf{k}}^{\dagger} e^{-\tau \hat{H}_0} = e^{\epsilon_k \tau} c_{\mathbf{k}}^{\dagger}, \tag{4.32}$$

$$c_{\mathbf{k}}(\tau) = e^{\tau \hat{H}_0} c_{\mathbf{k}} e^{-\tau \hat{H}_0} = e^{-\epsilon_k \tau} c_{\mathbf{k}}. \tag{4.33}$$

The Green's function can be evaluated as

$$\begin{aligned} G_0(\tau - \tau') =& - \langle \hat{T} c_{\mathbf{k}}(\tau) c_{\mathbf{k}}^{\dagger}(\tau') \rangle \\ =& - \left(\theta(\tau - \tau') \langle c_{\mathbf{k}} c_{\mathbf{k}}^{\dagger} \rangle \pm \theta(\tau' - \tau) \langle c_{\mathbf{k}}^{\dagger} c_{\mathbf{k}} \rangle \right). \end{aligned} \tag{4.34}$$

For fermions the Green's function is

$$G_0^F(\tau - \tau') = - \left(\theta(\tau - \tau') \left(1 - n_F(\epsilon_{\mathbf{k}})\right) - \theta(\tau' - \tau) n_F(\epsilon_{\mathbf{k}}) \right) e^{-\epsilon_{\mathbf{k}}(\tau - \tau')}, \tag{4.35}$$

and bosonic Green's function is

$$G_0^B(\tau - \tau') = - \left(\theta(\tau - \tau') \left(1 + n_B(\epsilon_{\mathbf{k}})\right) + \theta(\tau' - \tau) n_F(\epsilon_{\mathbf{k}}) \right) e^{-\epsilon_{\mathbf{k}}(\tau - \tau')}. \tag{4.36}$$

In the frequency space, the fermionic Green's function is

$$\begin{aligned} G_0^F(i\omega_n) =& \int_0^{\beta} d\tau e^{i\omega_n} G_0^F(\tau) \\ =& \left(n_F(\epsilon_{\mathbf{k}}) - 1\right) \frac{e^{i\omega_n \beta - \epsilon_{\mathbf{k}} \beta} - 1}{i\omega_n - \epsilon_{\mathbf{k}}} \\ =& \frac{1}{i\omega_n - \epsilon_{\mathbf{k}}}, \end{aligned} \tag{4.37}$$

where $\omega_n = (2n+1)\frac{\pi}{\beta}$. For the bosonic one, it has a similar form in the frequency space

$$\begin{aligned} G_0^B(i\nu_n) &= \int_0^\beta d\tau e^{i\nu} G_0^B(\tau) \\ &= -\left(n_B(\epsilon_{\mathbf{k}})+1\right)\frac{e^{i\nu_n\beta-\epsilon_{\mathbf{k}}\beta}-1}{i\nu_n-\epsilon_{\mathbf{k}}} \\ &= \frac{1}{i\nu_n-\epsilon_{\mathbf{k}}}, \end{aligned} \tag{4.38}$$

where $\nu_n = 2n\frac{\pi}{\beta}$.

4.5.2 Feynman Rules

The spin-orbit coupling can be understood by a scattering process with energy and momentum conserved as shown in the left side of Fig. 4.6. The on-site Coulomb interaction is shown in the right side of Fig. 4.6. Since the on-site Coulomb

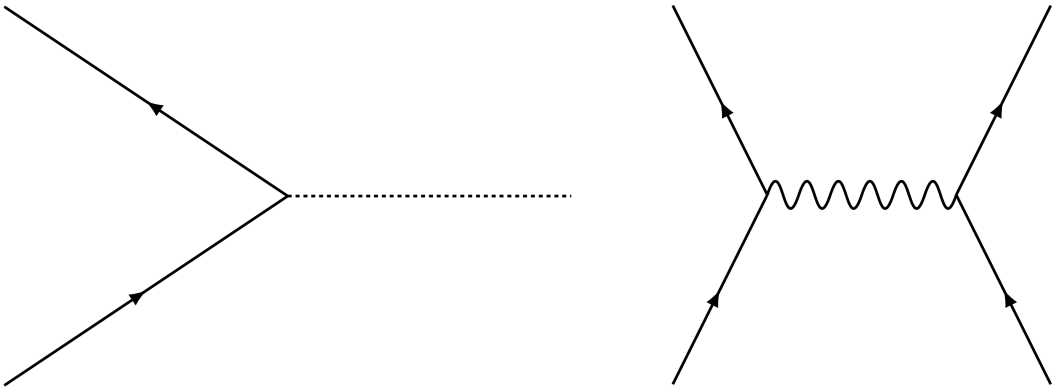

Figure 4.6: Feynman diagrams of the Spin-orbit coupling (left) and the Coulomb interaction (right).

interaction involves two electrons with different quantum numbers, it can involve spin-orbit scattering by playing an immediate process as shown in Fig. 4.7, which is a first-order correction to the spin-orbit coupling vertex. The enhancement of the

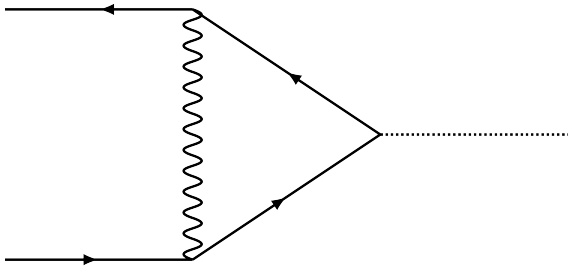

Figure 4.7: Feynman diagrams of the first-order spin-orbit coupling enhancement.

spin-orbit coupling can be evaluated by

$$\begin{aligned}\Delta\lambda_\gamma^{(1)} =& \frac{1}{\beta}\int \frac{d\mathbf{k}}{(2\pi)^3}\sum_{i\omega_n}(-U)\frac{1}{i\omega_n-\epsilon_{\mathbf{k},\alpha,\sigma}}\frac{1}{i\omega_n-\epsilon_{\mathbf{k},\beta,\sigma'}} \\ =& \int \frac{d\mathbf{k}}{(2\pi)^3}(-U)\frac{n_{\mathbf{k},\alpha,\sigma}-n_{\mathbf{k},\beta,\sigma'}}{\epsilon_{\mathbf{k},\alpha,\sigma}-\epsilon_{\mathbf{k},\beta,\sigma'}},\end{aligned} \tag{4.39}$$

where $n_{\mathbf{k},\alpha,\sigma}$ is occupation number of the electron of momentum $\mathbf{k}$, orbital α, and spin σ. If we sum the vertex correction to all orders, the fully renormalized spin-orbit coupling constant is

$$\lambda_\gamma = \frac{\lambda_0}{1+\int \frac{d\mathbf{k}}{(2\pi)^3}U\frac{n_{\mathbf{k},\alpha,\sigma}-n_{\mathbf{k},\beta,\sigma'}}{\epsilon_{\mathbf{k},\alpha,\sigma}-\epsilon_{\mathbf{k},\beta,\sigma'}}}. \tag{4.40}$$

The enhanced spin-orbit coupling evaluated from the Feynman diagrams is consistent with the numerical calculations in Fig. 4.4. When all bands are empty, there is no enhancement. When the bottom bands start to fill, but the corresponding upper bands are still empty, the enhancement gradually increases. However, while some corresponding upper bands are to be filled, the enhancement can be reduced. Finally, when all the bands are filled, there is no enhancement.

4.6 Conclusion

In conclusion, we have demonstrated the possibility that the Rashba spin-orbit coupling can be resonantly enhanced by Coulomb interaction and that the enhancement is highly nonlinear in the applied electric field. By tuning the chemical potential properly, it is possible to have giant Rashba couplings. Therefore, in strongly correlated materials, the observation of field-dependent Rashba coupling might have an explanation that is different from those that have been previously proposed for weakly interacting electron two-dimensional materials and, in some experiments, the observed giant Rashba coupling can be explained by the model proposed.

CHAPTER 5

CONCLUSION AND FUTURE PROPOSAL

In this dissertation, we have explicitly studied three cases of spin-orbit coupling in strongly correlated systems.

In the first case, nonmagnetic impurity states in topological Kondo insulators are studied. It is found that small imperfections in Kondo insulators can lead to the formation of in-gap bound states which have some similar properties to those of topological surface states. This can be utilized to explain the existence of surface conducting states in the first topological Kondo insulator SmB_6.

In the second one, a direct spin-orbit coupling enhancement due to strong Coulomb interaction is proposed to explain the unexpected strong spin-orbit coupling in $5f$ metals. It is shown that modest values of the Coulomb interaction can enhance the spin-orbit coupling by factors of about 4, which can have significant effects on the electronic spectrum. It is also suggested that anisotropic enhanced spin-orbit coupling might exist in non-cubic crystals.

In the last case, we study the Rashba spin-orbit coupling in a two-dimensional strongly correlated system. In our model, it is proved that there might exist a nonlinear Rashba effect on the surface of materials with strong correlation. It also explains the existence of giant Rashba constants observed in some experiments.

For a future perspective, it is desirable to examine how doping heavy elements which can lead to a strong Coulomb interaction into materials with moderate spin-orbit coupling effects to significantly change their properties. In that case, it might be possible to search for better materials applicable for spintronics devices.

BIBLIOGRAPHY

[1] John Hubbard. Electron correlations in narrow energy bands. *Proceedings of the Royal Society of London. Series A. Mathematical and Physical Sciences*, 276(1365):238–257, 1963.

[2] Yua A Bychkov and É I Rashba. Properties of a 2D electron gas with lifted spectral degeneracy. *JETP Letters*, 39(2):78, 1984.

[3] Aurelien Manchon, Hyun Cheol Koo, Junsaku Nitta, SM Frolov, and RA Duine. New perspectives for Rashba spin-orbit coupling. *Nature Materials*, 14(9):871–882, 2015.

[4] M Zahid Hasan and Charles L Kane. Colloquium: topological insulators. *Reviews of Modern Physics*, 82(4):3045, 2010.

[5] M Abele, X Yuan, and Peter S Riseborough. Topological nonmagnetic impurity states in topological Kondo insulators. *Physical Review B*, 101(9):094101, 2020.

[6] John R Schrieffer and Peter A Wolff. Relation between the Anderson and Kondo Hamiltonians. *Physical Review*, 149(2):491, 1966.

[7] Liang Fu, Charles L Kane, and Eugene J Mele. Topological insulators in three dimensions. *Physical Review Letters*, 98(10):106803, 2007.

[8] Maxim Dzero, Kai Sun, Victor Galitski, and Piers Coleman. Topological Kondo insulators. *Physical Review Letters*, 104(10):106408, 2010.

[9] Maxim Dzero, Jing Xia, Victor Galitski, and Piers Coleman. Topological Kondo insulators. *Annual Review of Condensed Matter Physics*, 7:249–280, 2016.

[10] Steven Wolgast, Çağlıyan Kurdak, Kai Sun, JW Allen, Dae-Jeong Kim, and Zachary Fisk. Low-temperature surface conduction in the Kondo insulator SmB_6. *Physical Review B*, 88(18):180405, 2013.

[11] DJ Kim, S Thomas, T Grant, J Botimer, Z Fisk, and Jing Xia. Surface Hall effect and nonlocal transport in SmB_6: evidence for surface conduction. *Scientific Reports*, 3(1):1–4, 2013.

[12] Nan Xu, Pabitra Kumar Biswas, Rajendra S Dhaka, Gabriel Landolt, Stefan Muff, Christian E Matt, Xun Shi, Nicholas C Plumb, M Radović, E Pomjakushina, et al. Direct observation of the spin texture in SmB_6 as evidence of the topological Kondo insulator. *Nature Communications*, 5(1):1–5, 2014.

[13] Peter Hlawenka, Konrad Siemensmeyer, Eugen Weschke, Andrei Varykhalov, Jaime Sánchez-Barriga, Natalya Y Shitsevalova, AV Dukhnenko, VB Filipov, Slavomir Gabáni, Karol Flachbart, et al. Samarium hexaboride is a trivial surface conductor. *Nature Communications*, 9(1):1–7, 2018.

[14] Xiao Yuan, Peter S Riseborough, EJ Calegari, and SG Magalhaes. Enhanced spin-orbit coupling in the underscreened Anderson lattice model for itinerant $5f$ metals. *Electronic Structure*, 3(2):024009, 2021.

[15] GH Lander, MSS Brooks, B Lebech, PJ Brown, O Vogt, and K Mattenberger. Measurement of giant magnetic anisotropy in a uranium compound. *Applied Physics Letters*, 57(10):989–991, 1990.

[16] TTM Palstra, AA Menovsky, J Van den Berg, AJ Dirkmaat, PH Kes, GJ Nieuwenhuys, and JA Mydosh. Superconducting and magnetic transitions in the heavy-fermion system URu_2Si_2. *Physical Review Letters*, 55(24):2727, 1985.

[17] Mirosław Werwiński, Jan Rusz, John A Mydosh, and Peter M Oppeneer. Exceptional ising magnetic behavior of itinerant spin-polarized carriers in URu_2Si_2. *Physical Review B*, 90(6):064430, 2014.

[18] AL Kutepov and SG Kutepova. The *ab initio* ground state properties and magnetic structure of plutonium. *Journal of Physics: Condensed Matter*, 15(17):2607, 2003.

[19] MT Butterfield, JG Tobin, NE Teslich, RA Bliss, MA Wall, AK McMahan, BW Chung, AJ Schwartz, and AL Kutepov. Utilizing nano-focussed bremstrahlung isochromat spectroscopy (nbis) to determine the unoccupied electronic structure of Pu. *MRS Online Proceedings Library*, 893(1):1–7, 2005.

[20] Hiroshi Yamagami and Akira Hasegawa. Self-consistent symmetrized relativistic augmented plane wave method: application to α-U. *Journal of the Physical Society of Japan*, 59(7):2426–2442, 1990.

[21] Takeo Ejima, Katsutoshi Murata, Shoji Suzuki, Takashi Takahashi, Shigeru Sato, Tadao Kasuya, Yoshichika Ōnuki, Hiroshi Yamagami, Akira Hasegawa, and Takehiko Ishii. Electronic structure of UC studied by X-ray photoemission and bremsstrahlung isochromat spectroscopy. *Physica B: Condensed Matter*, 186:77–79, 1993.

[22] J Trygg, JM Wills, MSS Brooks, B Johansson, and O Eriksson. Calculation of elastic constants in UC, US, and UTe. *Physical Review B*, 52(4):2496, 1995.

[23] A Hasegawa and H Yamagami. Electronic structures of plutonium monochalcogenides. *Journal of Magnetism and Magnetic Materials*, 104:65–66, 1992.

[24] Shin-ichi Fujimori, Yasuharu Saito, Masaharu Seki, Koji Tamura, Munenori Mizuta, Ken-ichiro Yamaki, Ken Sato, Akinori Tanaka, Noriaki Sato, Shoji Suzuki, et al. Absence of U $5f$ band states in resonant photoemission spectra of UPd_2Al_3. *Physical Review B*, 59(16):10469, 1999.

[25] Yves Baer and Jürg Kurt Lang. High-energy spectroscopic study of the occupied and unoccupied $5f$ and valence states in Th and U metals. *Physical Review B*, 21(6):2060, 1980.

[26] JG Tobin, KT Moore, BW Chung, MA Wall, AJ Schwartz, G van der Laan, and AL Kutepov. Competition between delocalization and spin-orbit splitting in the actinide $5f$ states. *Physical Review B*, 72(8):085109, 2005.

[27] JM Imer, D Malterre, M Grioni, P Weibel, B Dardel, and Y Baer. High-energy spectroscopy in uranium-based systems. *Physical Review B*, 44(19):10455, 1991.

[28] Natalia B Perkins, MD Nunez-Regueiro, Bernard Coqblin, and Jose Roberto Iglesias. Underscreened Kondo lattice model applied to heavy fermion uranium compounds. *Physical Review B*, 76(12):125101, 2007.

[29] J Schoenes, B Frick, and O Vogt. Transport properties of uranium monochalcogenide and monopnictide single crystals. *Physical Review B*, 30(11):6578, 1984.

[30] Christopher Thomas, Acirete S da Rosa Simoes, JR Iglesias, C Lacroix, NB Perkins, and B Coqblin. Application of the $S = 1$ underscreened Anderson lattice model to Kondo uranium and neptunium compounds. *Physical Review B*, 83(1):014415, 2011.

[31] B Coqblin, JR Iglesias, NB Perkins, Acirete S da R Simoes, and Christopher Thomas. Underscreened Kondo lattice model versus underscreened Anderson lattice model: Application to uranium compounds. *Physica B: Condensed Matter*, 404(19):2961–2963, 2009.

[32] Peter S Riseborough, B Coqblin, and SG Magalhaes. Phase transition arising from the underscreened Anderson lattice model: A candidate concept for explaining hidden order in URu_2Si_2. *Physical Review B*, 85(16):165116, 2012.

[33] Eleonir João Calegari, Sergio Garcia Magalhaes, and Peter S Riseborough. Unusual magnetic field-dependence of a possible hidden order phase. *npj Quantum Materials*, 2(1):1–9, 2017.

[34] John C Slater and George F Koster. Simplified LCAO method for the periodic potential problem. *Physical Review*, 94(6):1498, 1954.

[35] P Santini, Romuald Lemanski, and Paul Erdős. Magnetism of actinide compounds. *Advances in Physics*, 48(5):537–653, 1999.

[36] Philip Warren Anderson. Localized magnetic states in metals. *Physical Review*, 124(1):41, 1961.

[37] B Caroli, C Caroli, and DR Fredkin. Theory of spin resonance of localized moments in normal metals. *Physical Review*, 178(2):599, 1969.

[38] Lowell Dworin and Albert Narath. Orbital paramagnetism of localized nonmagnetic impurities in metals. *Physical Review Letters*, 25(18):1287, 1970.

[39] Laura M Roth. New method for linearizing many-body equations of motion in statistical mechanics. *Physical Review Letters*, 20(25):1431, 1968.

[40] PS Riseborough, SG Magalhaes, EJ Calegari, and G Cao. Enhancement of the spin-orbit coupling by strong electronic correlations in transition metal and light actinide compounds. *Journal of Physics: Condensed Matter*, 32(44):445601, 2020.

[41] JF Herbst, RE Watson, and I Lindgren. Coulomb term U and $5f$ electron excitation energies for the metals actinium to berkelium. *Physical Review B*, 14(8):3265, 1976.

[42] VN Antonov, BN Harmon, OV Andryushchenko, LV Bekenev, and AN Yaresko. Electronic structure and x-ray magnetic circular dichroism in uranium monochalcogenides. *Low Temperature Physics*, 30(4):305–316, 2004.

[43] Peter M Oppeneer, Jan Rusz, Saad Elgazzar, M-T Suzuki, T Durakiewicz, and JA Mydosh. Electronic structure theory of the hidden-order material URu_2Si_2. *Physical Review B*, 82(20):205103, 2010.

[44] Bernard Amadon. First-principles DFT+ DMFT calculations of structural properties of actinides: Role of Hund's exchange, spin-orbit coupling, and crystal structure. *Physical Review B*, 94(11):115148, 2016.

[45] Lin Miao, Shouzheng Liu, Yishuai Xu, Erica C Kotta, Chang-Jong Kang, Sheng Ran, Johnpierre Paglione, Gabriel Kotliar, Nicholas P Butch, Jonathan D Denlinger, et al. Low energy band structure and symmetries of UTe_2 from angle-resolved photoemission spectroscopy. *Physical Review Letters*, 124(7):076401, 2020.

[46] Ruizhi Qiu, Bingyun Ao, and Li Huang. Effective Coulomb interaction in actinides from linear response approach. *Computational Materials Science*, 171:109270, 2020.

[47] Towfiq Ahmed, Robert C Albers, Alexander V Balatsky, Christoph Friedrich, and Jian-Xin Zhu. GW quasiparticle calculations with spin-orbit coupling for the light actinides. *Physical Review B*, 89(3):035104, 2014.

[48] Haruhiko Ogasawara, Akio Kotani, and Bernard T Thole. Calculation of magnetic x-ray dichroism in $4d$ and $5d$ absorption spectra of actinides. *Physical Review B*, 44(5):2169, 1991.

[49] Per Söderlind, Olle Eriksson, Börje Johansson, JM Wills, and AM Boring. A unified picture of the crystal structures of metals. *Nature*, 374(6522):524–525, 1995.

[50] Igor Žutić, Jaroslav Fabian, and S Das Sarma. Spintronics: Fundamentals and applications. *Reviews of Modern Physics*, 76(2):323, 2004.

[51] Hongki Min, JE Hill, Nikolas A Sinitsyn, BR Sahu, Leonard Kleinman, and Allan H MacDonald. Intrinsic and Rashba spin-orbit interactions in graphene sheets. *Physical Review B*, 74(16):165310, 2006.

[52] Daniel Huertas-Hernando, F Guinea, and Arne Brataas. Spin-orbit coupling in curved graphene, fullerenes, nanotubes, and nanotube caps. *Physical Review B*, 74(15):155426, 2006.

[53] Junsaku Nitta, Tatsushi Akazaki, Hideaki Takayanagi, and Takatomo Enoki. Gate control of spin-orbit interaction in an inverted $In_{0.53}Ga_{0.47}As/In_{0.52}Al_{0.48}$ as heterostructure. *Physical Review Letters*, 78(7):1335, 1997.

[54] D Maryenko, M Kawamura, Arthur Ernst, VK Dugaev, E Ya Sherman, M Kriener, MS Bahramy, Y Kozuka, and M Kawasaki. Interplay of spin-orbit coupling and Coulomb interaction in ZnO-based electron system. *Nature Communications*, 12(1):1–6, 2021.

[55] Guang-Hong Chen and ME Raikh. Exchange-induced enhancement of spin-orbit coupling in two-dimensional electronic systems. *Physical Review B*, 60(7):4826, 1999.

[56] Christian R Ast, Jürgen Henk, Arthur Ernst, Luca Moreschini, Mihaela C Falub, Daniela Pacilé, Patrick Bruno, Klaus Kern, and Marco Grioni. Giant spin splitting through surface alloying. *Physical Review Letters*, 98(18):186807, 2007.

[57] D Marchenko, A Varykhalov, MR Scholz, G Bihlmayer, EI Rashba, A Rybkin, AM Shikin, and O Rader. Giant Rashba splitting in graphene due to hybridization with gold. *Nature Communications*, 3(1):1–6, 2012.

[58] PDC King, Richard C Hatch, Marco Bianchi, R Ovsyannikov, C Lupulescu, G Landolt, B Slomski, JH Dil, Dandan Guan, JL Mi, et al. Large tunable rashba spin splitting of a two-dimensional electron gas in Bi_2Se_3. *Physical Review Letters*, 107(9):096802, 2011.

[59] Hadj M Benia, Chengtian Lin, Klaus Kern, and Christian R Ast. Reactive chemical doping of the Bi_2Se_3 topological insulator. *Physical Review Letters*, 107(17):177602, 2011.

[60] AF Santander-Syro, F Fortuna, C Bareille, TC Rödel, G Landolt, NC Plumb, M Radović, et al. Giant spin splitting of the two-dimensional electron gas at the surface of $SrTiO_3$. *Nature Materials*, 13(12):1085–1090, 2014.

[61] J Henk, A Ernst, and P Bruno. Spin polarization of the L-gap surface states on Au (111). *Physical Review B*, 68(16):165416, 2003.

[62] G Nicolay, F Reinert, S Hüfner, and P Blaha. Spin-orbit splitting of the L-gap surface state on Au (111) and Ag (111). *Physical Review B*, 65(3):033407, 2001.

[63] Friedrich Reinert. Spin-orbit interaction in the photoemission spectra of noble metal surface states. *Journal of Physics: Condensed Matter*, 15(5):S693, 2003.

[64] Lars Petersen and Per Hedegård. A simple tight-binding model of spin-orbit splitting of *sp*-derived surface states. *Surface Science*, 459(1-2):49–56, 2000.

[65] Hong Yang, Xiangyang Peng, Wenliang Liu, Xiaolin Wei, Guolin Hao, Chaoyu He, Jin Li, G Malcolm Stocks, and Jianxin Zhong. Electric tuning of the surface and quantum well states in Bi_2Se_3 films: a first-principles study. *Journal of Physics: Condensed Matter*, 26(39):395005, 2014.

[66] S LaShell, BAa McDougall, and E Jensen. Spin splitting of an Au (111) surface state band observed with angle resolved photoelectron spectroscopy. *Physical Review Letters*, 77(16):3419, 1996.

APPENDIX A

DIRAC EQUATION

A.1 Spin-orbit Coupling Emerging from Dirac Equation

Write down single-particle Dirac equation with mass m

$$(\gamma^{\mu} k_{\mu} - m)\Psi = 0. \tag{A.1}$$

Choose the standard matrix representation of Gamma matrices as

$$\gamma^{0} = \begin{pmatrix} \hat{I} & 0 \\ 0 & -\hat{I} \end{pmatrix}, \tag{A.2}$$

and

$$\gamma^{\mu} = \begin{pmatrix} 0 & \sigma^{i} \\ -\sigma^{i} & 0 \end{pmatrix}. \tag{A.3}$$

The Dirac equation can be written in the matrix form as

$$\begin{pmatrix} (k^0 - m)\hat{I} & -k^i\sigma^i \\ k^i\sigma^i & (k^0 + m)\hat{I} \end{pmatrix} \begin{pmatrix} \varphi^+ \\ \varphi^- \end{pmatrix} = 0, \tag{A.4}$$

which explicitly has the spin-orbit coupling term. Under the transformation $m \to -m$, the wave function transforms as

$$\Psi \to \begin{pmatrix} 0 & \hat{I} \\ \hat{I} & 0 \end{pmatrix} \Psi, \tag{A.5}$$

which interchanges the upper two-component spinor with the lower one. The eigenvalues are invariant under the mass inversion. At $\mathbf{k} = 0$, the mass inversion leads to the parity change of the wave function, which makes it promising in describing topological insulators.

Consider a thin film of topological insulator with the mass depending on the spatial coordinates z

$$m(z) = m\left(1 - 2\Theta(z + a) + 2\Theta(z - a)\right). \tag{A.6}$$

In the limit $a \to \infty$, in-gap states have a gapless dispersion relation

$$k_0 = \tau|\mathbf{k}_\parallel|, \tag{A.7}$$

where $\tau = \pm 1$. The effective Hamiltonian can have the form of a Rashba Hamiltonian, which is the manifestation of spin-momentum locking.

A.2 Spherical Void in Topological Insulators

A spherical void in a topological insulator can be described by the Dirac equation, in which the mass $m(r)$ depends on the radial distance. The spinors can be represented by

$$\Psi = \frac{1}{r}\begin{pmatrix} f(r)\Omega_{j,j_z}^{j\pm\frac{1}{2}} \\ ig(r)\Omega_{j,j_z}^{j\mp\frac{1}{2}} \end{pmatrix} \tag{A.8}$$

in which the orbital angular momentum is given by $l = j \pm \frac{1}{2}$ and where the two-component spinor spherical harmonics are given by

$$\Omega_{j,j_z}^{j\pm\frac{1}{2}} = -\sqrt{\frac{j+1-j_z}{2j+2}}Y_{j_z-\frac{1}{2}}^{j+\frac{1}{2}}(\theta,\varphi)\begin{pmatrix}1\\0\end{pmatrix} + \sqrt{\frac{j+1+j_z}{2j+2}}Y_{j_z+\frac{1}{2}}^{j+\frac{1}{2}}(\theta,\varphi)\begin{pmatrix}0\\1\end{pmatrix} \tag{A.9}$$

and

$$\Omega_{j,j_z}^{j\pm\frac{1}{2}} = \sqrt{\frac{j+j_z}{2j}}Y_{j_z-\frac{1}{2}}^{j-\frac{1}{2}}(\theta,\varphi)\begin{pmatrix}1\\0\end{pmatrix} + \sqrt{\frac{j-j_z}{2j}}Y_{j_z+\frac{1}{2}}^{j-\frac{1}{2}}(\theta,\varphi)\begin{pmatrix}0\\1\end{pmatrix}. \tag{A.10}$$

The upper and lower components of the Dirac spinors have different l values and, therefore, have different parities. The spinor spherical harmonics are related by the identity

$$\left(\frac{\sigma^i r^i}{r}\right)\Omega_{j,j_z}^{j+\frac{1}{2}} = -\Omega_{j,j_z}^{j-\frac{1}{2}}. \tag{A.11}$$

The radial functions $f(r)$ and $g(r)$ satisfy the following coupled equations

$$\left(E - U(r) - m(r)\right)f(r) - \left(\frac{\partial}{\partial r} - \frac{\kappa}{r}\right)g(r) = 0, \tag{A.12}$$

$$\left(E - U(r) + m(r)\right)f(r) + \left(\frac{\partial}{\partial r} + \frac{\kappa}{r}\right)g(r) = 0, \tag{A.13}$$

where $\kappa = \pm(j + \frac{1}{2})$. The energy eigenstates of the spherically symmetric Dirac equation are classified by the three quantum numbers (j, j_z, κ). Consider the mass term of the form

$$m(r) = M - (M + m)\Theta(r - a), \tag{A.14}$$

such that the system is topologically nontrivial in the region where $r > a$ and topologically trivial in the region $r < a$. The spherical boundary at $r = a$ separates the void from the topological insulator. The potential is set to be nonzero inside the void

$$U(r) = \Delta U \Theta(a - r). \tag{A.15}$$

Since the mass term and the potential are constant in either region, we can simply define the radial quantum numbers for each region by

$$(E - \Delta U)^2 - M^2 = k_<^2, \tag{A.16}$$

$$E^2 - m^2 = k_>^2. \tag{A.17}$$

The bulk states correspond to positive values of k while the in-gap states are found by analytically continuing k to imaginary values. For simplicity, we express the solutions in terms of the dimensionless variable $\rho = kr$. The solutions in the two regions satisfy the Riccatti-Bessel equation

$$f(\rho) = A\sqrt{\rho} Z_{|\kappa + \frac{1}{2}|}, \tag{A.18}$$

$$g(\rho) = B\sqrt{\rho} Z_{|\kappa - \frac{1}{2}|}, \tag{A.19}$$

which are of the form of Bessel functions of half-integer order. For $r > a$, normalizability requires the solutions are Bessel functions of the first kind, $Z_{|\kappa \pm \frac{1}{2}|} = J_{|\kappa \pm \frac{1}{2}|}$.The

Bessel function recursion relations

$$J_{\nu-1} + J_{\nu+1} = \frac{2\nu}{\rho} J_\nu, \tag{A.20}$$

$$J_{\nu-1} - J_{\nu+1} = 2\frac{\partial J_\nu}{\partial \rho}, \tag{A.21}$$

for $\nu > 0$, can be used to yield the relation between the amplitudes of the upper and lower components

$$\left(\frac{E - \Delta U - M}{k_<}\right) A_< = -\operatorname{sgn}(\kappa) B_<. \tag{A.22}$$

Since we are interested in the in-gap states, the solutions in the exterior region are restricted to the Hankel functions $H^{(1)}_{|\kappa \pm \frac{1}{2}|}$ with an asymptotic variation of

$$H^{(1)}_{|\kappa \pm \frac{1}{2}|}(\rho) \sim \frac{1}{\sqrt{\rho}} \exp(i\rho), \tag{A.23}$$

which is exponentially decaying when $k_>$ is analytically continued to imaginary values. The Bessel function recursion relations also lead to relation between the amplitudes of the upper and lower components

$$\left(\frac{E + m}{k_>}\right) A_> = -\operatorname{sgn}(\kappa) B_>. \tag{A.24}$$

The continuity of the wave function at $r = a$ leads to the equation

$$\left(\frac{E - \Delta U + M}{k_<}\right) \left(\frac{j_{|\kappa+\frac{1}{2}|-\frac{1}{2}}(k_< a)}{j_{|\kappa-\frac{1}{2}|-\frac{1}{2}}(k_< a)}\right) = \left(\frac{E - m}{k_>}\right) \left(\frac{h^{(1)}_{|\kappa+\frac{1}{2}|-\frac{1}{2}}(k_> a)}{h^{(1)}_{|\kappa-\frac{1}{2}|-\frac{1}{2}}(k_> a)}\right) \tag{A.25}$$

which are expressed in terms of the spherical Bessel functions. Therefore, the eigenstates are degenerate with respect to j_z and the energy can only depend on j and on

the parity of $(-1)^{|\kappa+\frac{1}{2}|-\frac{1}{2}}$. The spherical Bessel functions are defined by

$$j_v(\rho) = \sqrt{\frac{\pi}{2\rho}} J_{\nu+\frac{1}{2}}(\rho), \tag{A.26}$$

$$h_v^{(1)}(\rho) = \sqrt{\frac{\pi}{2\rho}} H^{(1)}_{\nu+\frac{1}{2}}(\rho). \tag{A.27}$$

The first few analytic continued spherical Bessel functions are given in Table A.1.

ν	$j_\nu(ix)$	$h_\nu^{(1)}(ix)$
0	$\frac{\sinh x}{x}$	$-\frac{e^{-x}}{x}$
1	$i\left(\frac{x\cosh x - \sinh x}{x^2}\right)$	$i\frac{e^{-x}}{x}\left(\frac{1+x}{x}\right)$
2	$-\left(\frac{(3+x^2)\sinh x - 3x\cosh x}{x^3}\right)$	$\frac{e^{-x}}{x}\left(\frac{3+3x+x^2}{x^2}\right)$
3	$-i\left(\frac{(15x+x^3)\cosh x - (15+6x^2)\sinh x}{x^4}\right)$	$-i\frac{e^{-x}}{x}\left(\frac{15+15x+6x^2+x^3}{x^3}\right)$
4	$\left(\frac{(105+45x^2+x^4)\sinh x - (105x+10x^3)\cosh x}{x^5}\right)$	$-\frac{e^{-x}}{x}\left(\frac{105+105x+45x^2+10x^3+x^4}{x^4}\right)$

Table A.1: The first few spherical Bessel functions continued to imaginary arguments.

The in-gap state eigenequation only has positive energy solutions for positive values of κ, with $\kappa = j + \frac{1}{2}$, as expected from the band inversion in a topological insulator. Therefore, the surface states can be uniquely characterized by the sign of their energies and (j, j_z). As a result, the surface states have lost half their degrees of freedom, due to the locking of the spin with orbital angular momentum. The bound state energies as a function of the radius a are plotted in Fig. A.1 and the probability distributions for $j = \frac{1}{2}$ are shown in Fig. A.2.

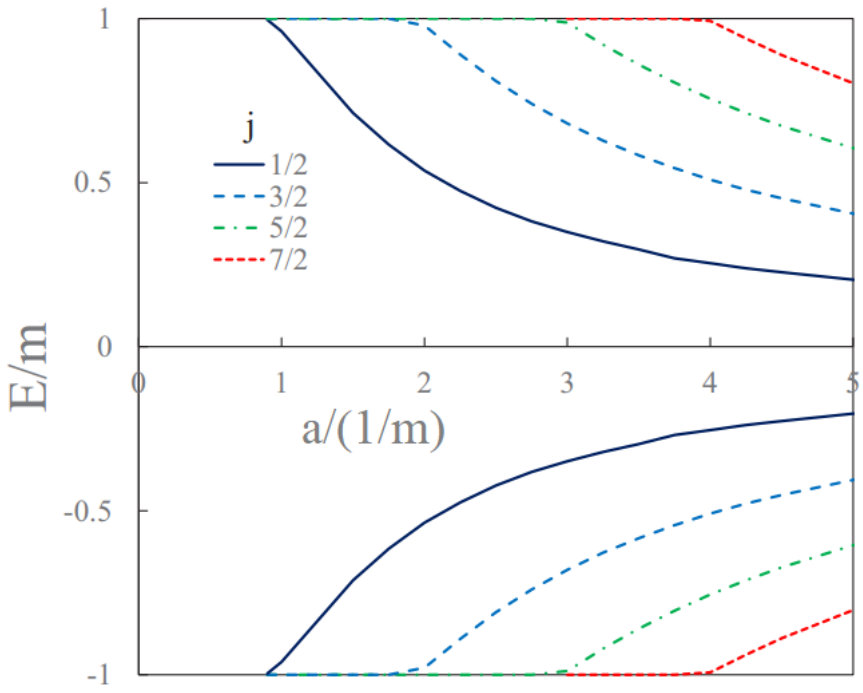

Figure A.1: The bound state energies for different j as functions of the ratio of the radius a to the decay length $1/m$.

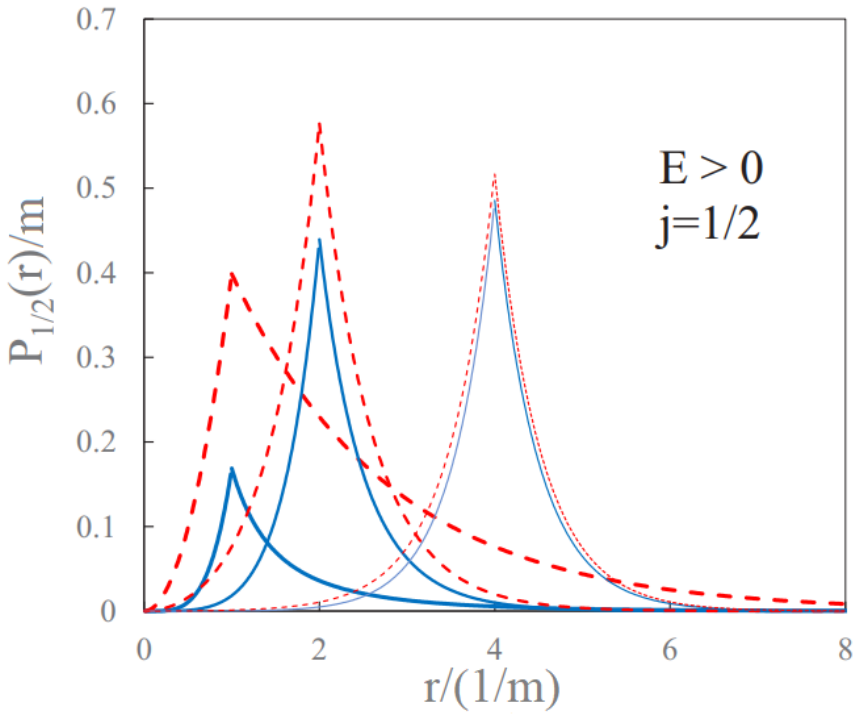

Figure A.2: The radial distribution functions for the upper components ($l = 1$ solid blue) and lower components ($l = 0$ dashed red) of the $j = \frac{1}{2}$ positive energy bound state for $a = 1$ (thick), $a = 2$ (medium), and $a = 4$ (fine).